Geophys. J. R. astr. Soc. (1986) **86**, 331–369

Crustal structure in the Western Somali Basin

Millard F. Coffin* *Department of Geological Sciences, Columbia University, New York, NY 10025, USA, and Lamont–Doherty Geological Observatory, Palisades, NY 10964, USA*

Philip D. Rabinowitz *Lamont–Doherty Geological Observatory, Palisades, NY 10964, USA and Ocean Drilling Program, Texas A & M University, College Station, TX 77843, USA*

Robert E. Houtz *Chevron Oil Field Research Company, PO Box 446, La Habra, CA 90631, USA*

Accepted 1986 January 2. Received 1986 January 2; in original form 1985 May 17

Summary. As part of integrated marine geophysical studies in the Western Somali Basin, we performed 118 sonobuoy experiments to define better the crustal structure of the margins and basin created by the separation of Madagascar and Africa. After using T^2/X^2, conventional slope-intercept methods, and slant-stacked τ-p techniques to analyse the data, we combined our solutions with all previous velocity information for the area. Velocity functions were derived for the sediment column, and we detected a high-velocity (4.58 ± 0.29 km s^{-1}) sediment layer overlying acoustic basement. We confirmed that the crust is indeed seismically oceanic, and that it may be considered either in terms of a layered model – layers 2B (5.42 ± 0.19 km s^{-1}), 2C (6.23 ± 0.22 km s^{-1}), 3 (7.03 ± 0.25 km s^{-1}), and mantle (7.85 ± 0.32 km s^{-1}) were identified – or a more complex gradient model in which layer 2 is marked by a steeper velocity gradient than underlying layer 3. Integrated igneous crustal thicknesses (1.62 ± 0.22 s, 5.22 ± 0.64 km) are significantly less than what is considered normal. We present a revised seismic transect across the East African margin, as well as total sediment thickness, depth to basement and crustal thickness maps.

Key words: crustal structure, East Africa, Madagascar, sonobuoy, $\tau - p$ inversion

Introduction

The nature of the crust underlying the Western Somali and Comoros basins in the western Indian Ocean has long been enigmatic (Fig. 1). Not a single drill hole in either basin has

* Now at: Bureau of Mineral Resources, Geology and Geophysics, GPO Box 378, Canberra, ACT 2601, Australia.

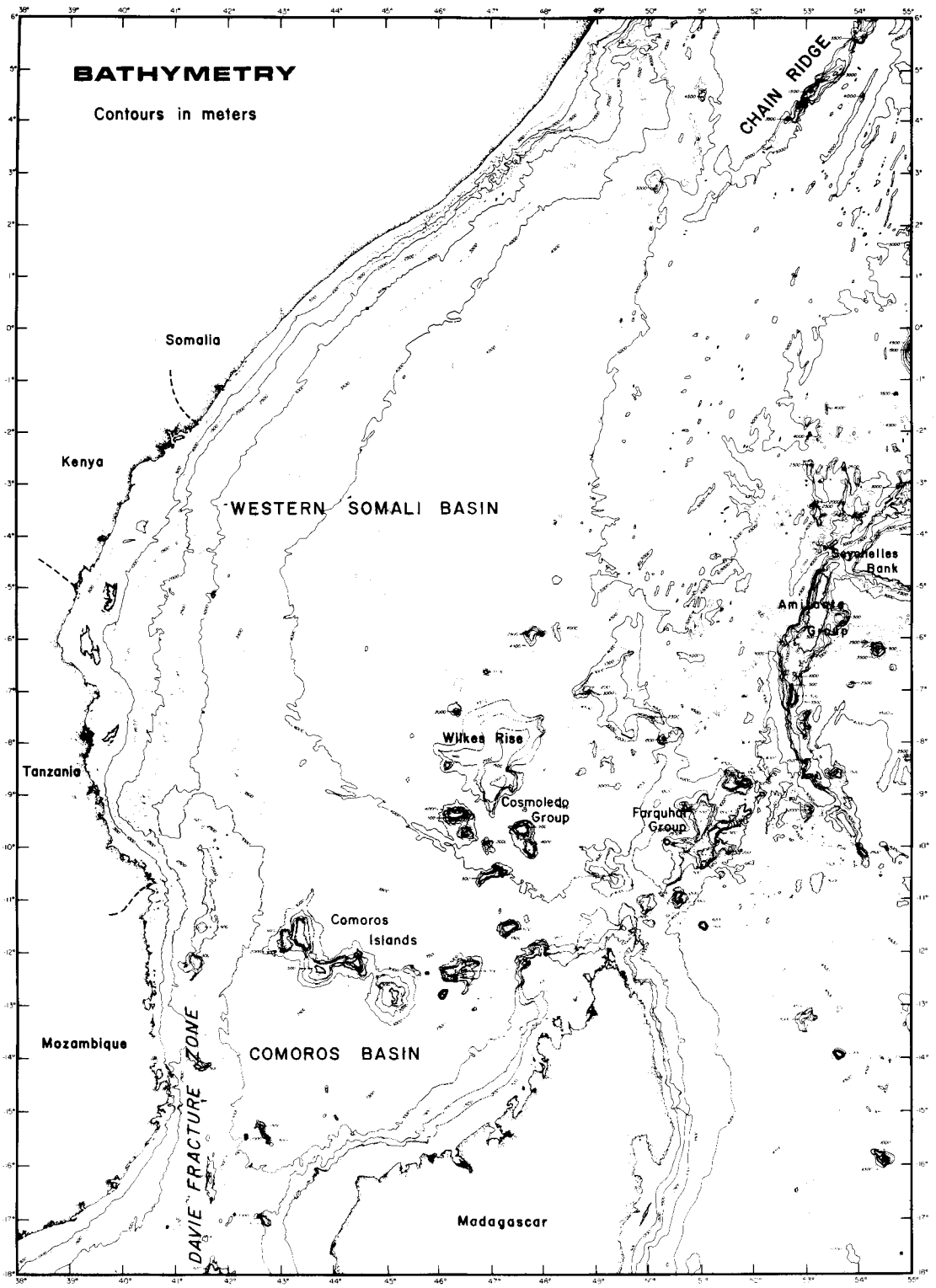

Figure 1

reached unambiguous igneous basement. The only major seismic investigation prior to 1980 consisted of seven sonobuoy experiments in the Western Somali Basin (Francis 1964; Francis, Davies & Hill 1966) and produced indefinite results; rocks with velocities typical for basal crustal rocks beneath both oceans and continents (6.6–7.2 km s^{-1}) were determined to extend eastward from Kenya to approximately 47°E longitude in the Western Somali Basin (Fig. 2, upper). Four sonobuoy experiments in the Comoros Basin (Lort *et al.* 1979) resulted in similar ambiguity. They speculated that the roughly east–west trend of the Comoros Islands at ~ 11°S latitude marked the boundary between oceanic crust to the north (Western Somali Basin) and continental crust to the south (Comoros Basin).

The recent discovery and identification of marine magnetic anomalies of Mesozoic age in the Western Somali and Comoros basins apparently resolves any questions about the crustal nature of these basins (Fig. 3) (Rabinowitz, Coffin & Falvey 1983). Yet the seismic structure of both basins remained ill-defined and unresolved. From 1980 November to 1981 January, the final scientific voyage of R/V *Vema* was devoted to researching the evolution of the Western Somali and Comoros basins, and the East African continental margin. As one facet of integrated geophysical studies we performed 118 sonobuoy wide-angle reflection and refraction experiments with a principal objective of better defining the crustal structure of these basins. We describe here the results obtained through various analytical methods.

The study area (Fig. 1) comprises the Western Somali Basin; Mesozoic marine magnetic anomalies and the Jurassic Magnetic Quiet Zone date the crust in this area as Middle Jurassic through Hauterivian (Fig. 3). Emerick & Duncan (1982) have convincingly shown that the Comoros Islands were formed by age-progressive volcanism over the past 10 Myr, from ~ 10 Myr volcanics at Diego Suarez on the north-eastern tip of Madagascar to recent volcanics on Grande Comore Island, the westernmost of the group. Thus for the vast majority of the Western Somali and Comoro basins' history, they comprised one basin that was created during the early break-up of Gondwanaland. The tectonic scenario for the area involves north–south relative motion between Madagascar (attached to India, Anarctica and Australia at the time) and Africa, with the Davie Fracture Zone forming the western transform fault. Seafloor spreading began during the Jurassic Magnetic Quiet Zone, and ceased at anomaly M10, or ~ 130 Ma (Rabinowitz *et al.* 1983; Kent & Gradstein 1985). The margins bordering the Western Somali and Comoros basins are thus of two types: north-eastern Kenya/Somalia and northern Madagascar are conjugate passive rift margins, and south-eastern Kenya/Tanzania/north-eastern Mozambique and western Madagascar are conjugate passive transform margins.

Data acquisition and reduction

During R/V *Vema* legs V3618 and V3619 in the Western Somali and Comoros basins we performed 118 sonobuoy experiments, labelled nnnV36 in Fig. 4. In addition we obtained data from eight sonobuoy experiments conducted on R/V *Conrad* leg C1215 (nnnC12 in Fig. 4). Two large-volume (7.6 litres) airguns fired approximately every 50 m comprised the sound source for 107 of the experiments (322V36 to 436V36 and 449V36 to 462V36, inclusive). The other 11 R/V *Vema* experiments plus the eight additional R/V *Conrad* sonobuoys employed one 0.41 litre airgun. The data from 87 experiments (322V36 to 428V36, inclusive) were recorded digitally (see Figs 5a–9a for sample time–distance plots) simultaneously with multichannel seismics on a Texas Instruments DFS IV system at a 4 ms sampling interval.

Figure 1. Bathymetry of the East African continental margin, Madagascan insular margin, Western Somali Basin, and Comoros Basin. The contour interval is 500 m, and the data were corrected for variations in water velocity (Matthews 1939).

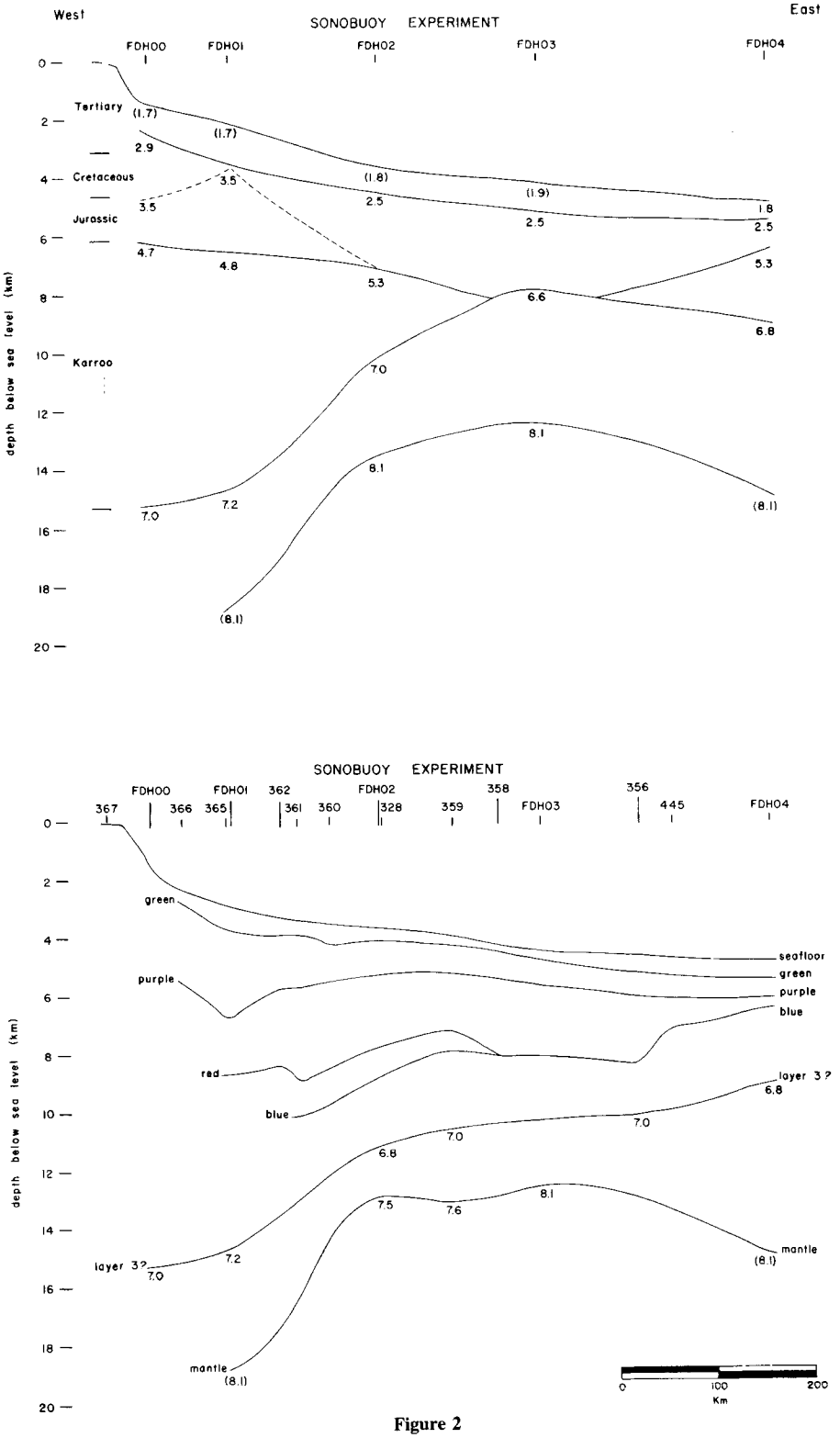

Figure 2

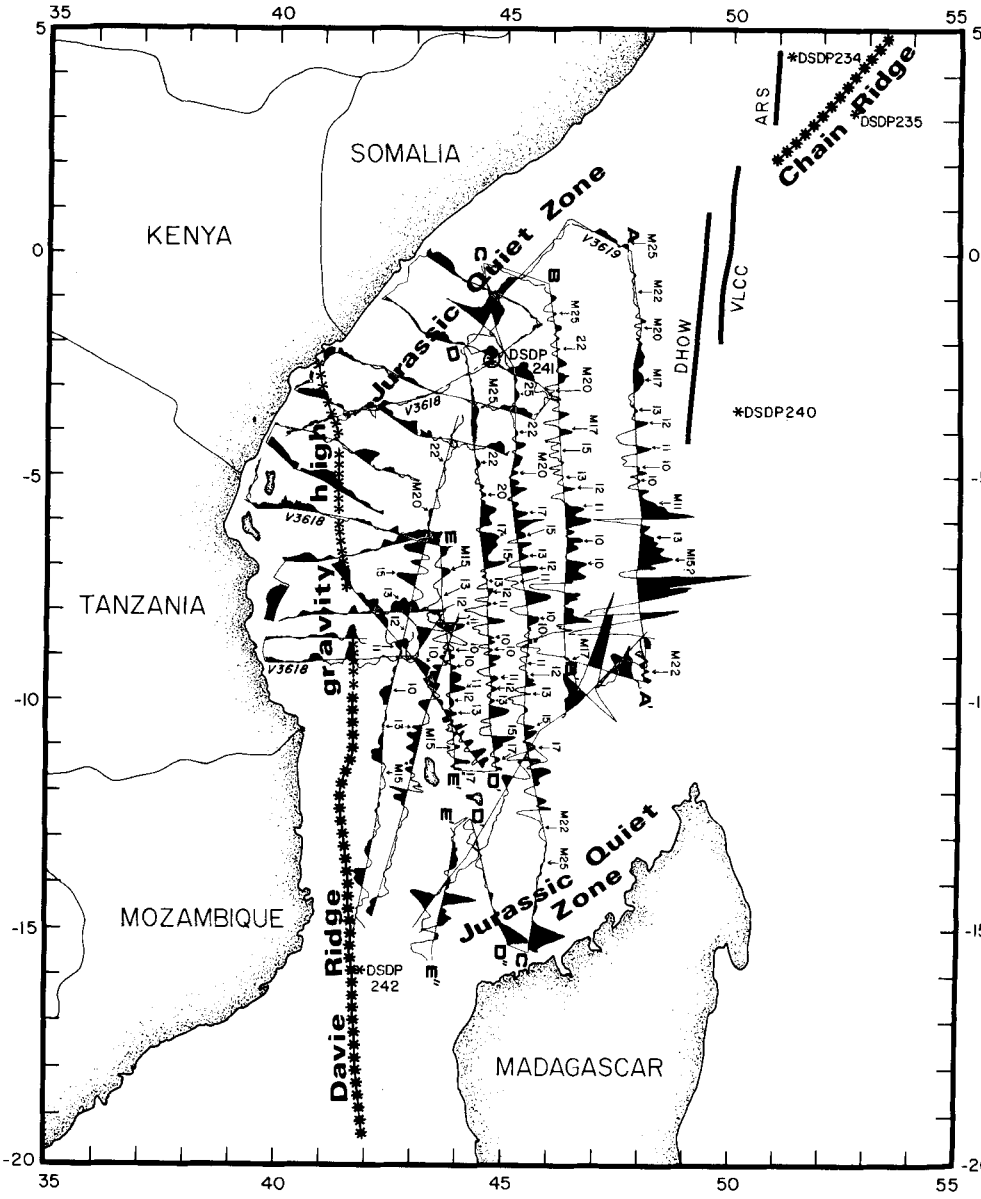

Figure 3. Magnetic anomaly identifications and tectonic elements in the Western Somali and Comoros basins.

Figure 2. Seismic transects of the East African continental margin. Experiment locations are given in Fig. 4, and velocities are conventional slope-intercept refraction solutions (Tables 1 and 2) in km s^{-1}. Values in parentheses are assumed refraction velocities. The vertical exaggeration is 30 : 1. (Upper) Section after Francis *et al.* (1966). The geological column at the left was provided by British Petroleum. (Lower) Revised section incorporating both the data of Francis *et al.* (1966) and those reported on in this paper. The reflectors are defined in Fig. 11, and the ages of the sediment units are as follows: green to seafloor is late Oligocene to Holocene; purple to green is mid-Cretaceous (?) to Middle Eocene; red to purple is Jurassic (?) to mid-Cretaceous (?); and blue to red is basement to Jurassic (?). Blue is acoustic, presumably igneous basement, and ranges from Middle Jurassic to Early Cretaceous in age over the entire Western Somali Basin. The mantle as well as the probable top of oceanic layer 3 are also identified.

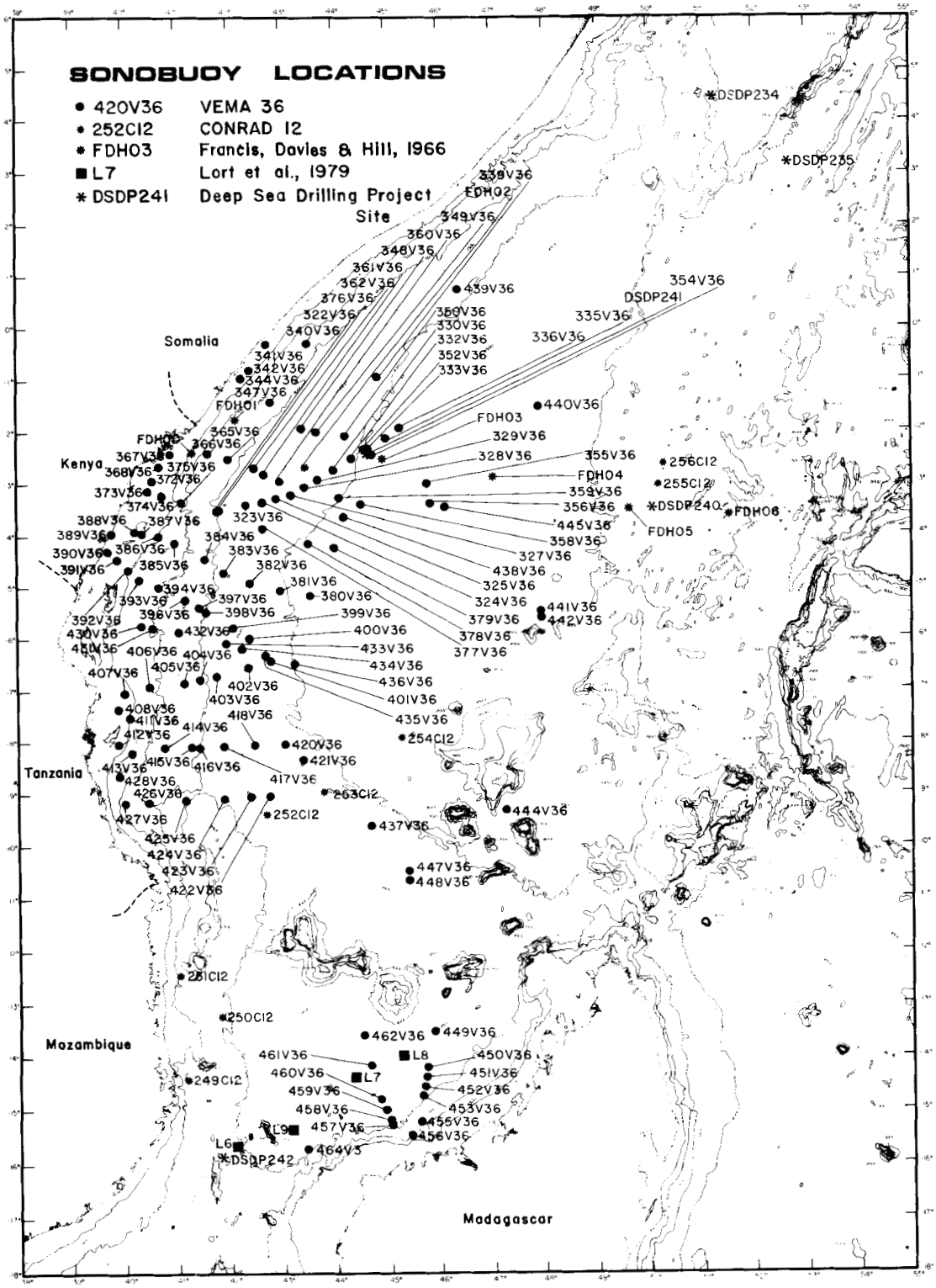

Figure 4

The other 39 experiments (430V36 to 464V36 and 249C12 to 256C12, inclusive) were analogue-recorded.

The data acquired during the *Vema* sonobuoy experiments were subject to the major source of error inherent in most such experiments, namely sonobuoy drift. Proximal to the East African coast this problem was severe, as we encountered Somali Current velocities of several knots to the NE and a counter-current seaward with similar velocities to the SW. In the same region constant ship speed over the seafloor was extremely difficult to maintain, violating our assumptions of constant shot spacing. In the absence of direct water arrivals, or *D*-waves on the seismograms (see Figs 5a and 9a for prominent *D*-waves), the range aspect resulting from these problems was often difficult to resolve satisfactorily and the data are of dubious quality. Nearly all of our sonobuoy experiments on the continental shelf and upper slope of East Africa fall into this category, and they have been deleted from any analysis beyond interval velocity and layer thickness determination.

The travel-time data from the 126 Lamont–Doherty experiments were analysed, whenever possible, by both a T^2/X^2 technique (Le Pichon, Ewing & Houtz 1968) and a slope-intercept method (Ewing 1963). Velocities were determined independently via both techniques from the same record section. Both methods assume planar interfaces between isotropic layers of constant velocity. Although variable-angle reflection data usually do not extend to oceanic crustal levels, the T^2/X^2 technique maintains three important advantages over the slope-intercept method: (1) velocity inversions can sometimes be discerned, (2) random dips can be accounted for in the absence of reversed profiles (none of our 126 profiles were reversed), and (3) the solutions are relatively insensitive to undetected changes of the ship's speed, an especially important feature on the shelf and upper slope in this area. Therefore, results from the sedimentary layers obtained by the former technique are weighted more in the final interpretation. Velocities and calculated layer thicknesses to the deepest observed refraction combining T^2/X^2 and slope-intercept analyses are tabulated in Table 1. The digitally recorded data shot with large-volume airguns were of excellent quality, with ranges exceeding 35 km (see Figs 5a to 9a for time–distance plots of five buoys). The letter 'R' in Table 1 indicates sonobuoy solutions which have been reconciled to the observed depth to mantle on multichannel seismic reflection data.

Five sonobuoys deployed over relatively flat seafloor and subseafloor horizons were chosen from the high-quality digital data set shot with large-volume airguns and further analysed in order to resolve the velocity structure of the lower sediment column and uppermost oceanic crust better (Figs 4 and 10). The combined T^2/X^2 and slope-intercept solutions were first modelled by constant-velocity layer ray-tracing and compared with the experimental data, and then adjusted until close agreement prevailed. The time–distance (X–T) data from these five sonobuoys were next transformed into the domain of intercept time (τ) and horizontal ray parameter (p) (Figs 5b–9b), according to the method of Stoffa *et al.* (1981). The transformed data were finally inverted via the τ-sum technique of Diebold (1980) and Diebold & Stoffa (1981), providing velocity–depth functions which are superimposed on the multichannel seismic profile along which the individual sonobuoy was deployed (Figs 5c–9c). A brief description of the procedure, similar to that of Stoffa *et al.* (1981), follows.

In transforming the X–T data into the τ–p domain, the data were first divided into overlapping subarrays. The length of these subarrays varied with source–receiver offset,

Figure 4. Sonobuoy wide-angle reflection and refraction stations and Deep Sea Drilling Project sites in the study area.

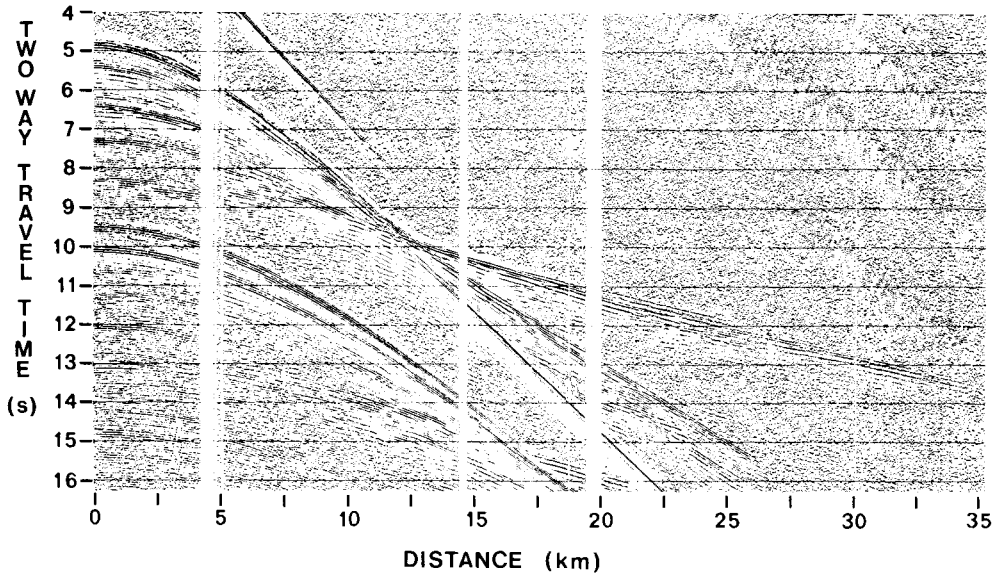

Figure 5. (a) The observational time–distance data for sonobuoy 325V36, with time-varying gain applied. (b) The τ–p map for sonobuoy 325V36, using the transformation technique of Stoffa *et al.* (1981). (c) The τ-sum inversion for sonobuoy 325V36, using the method of Diebold & Stoffa (1981). The inversion is superimposed on coinciding multichannel seismic reflection profile 81V (Fig. 10).

ranging from ~2.0 km at proximal offsets to ~4.0 km at distal offsets. Increasing the subarray length (synthetic aperture) at far offsets results in improved ray parameter resolution (Mutter 1982; Mutter, Talwani & Stoffa 1984). The overlap of each subarray with adjacent subarrays was generally 50 per cent. The original X–T data were bandpass-filtered between 6 and 20 Hz with cosine tapers of 3 Hz (low end) and 10 Hz (high end). For each subarray a ray parameter (slowness) stack for linear trajectories through the X–T data was performed for ray parameters between 0.020 and 0.660 s km^{-1} in increments of 0.005 s km^{-1}. Semblance for each subarray was also calculated. A major problem of slowness-stacking is spatial aliasing, and the semblance, after being filtered 0–5 Hz with a cosine taper of 5 Hz (high end), was used to derive a window function that we applied to the slowness stacks. A semblance minimum of 0.1 was employed, and it produced a strong trace of refractions and post-critical reflections. Original bandwidth was preserved, and true-amplitude, suppressed-aliased τ–p stacks for each subarray were obtained. The slowness stacks for all of the subarrays were then summed and Hilbert-transformed, resulting in band-pass filtered τ–p maps for each of the five sonobuoys shown in Figs 5(b)–9(B) and 10. No time window was applied to the X–T (Figs 5a–9a) or τ–p (Figs 5b–9b) data to eliminate water column multiple energy. In none of the five cases did this energy impinge upon the energy band utilized for the τ-sum inversions (Figs 5c–9c).

Velocity–depth functions were obtained through inversion of the τ–p data using the τ-sum technique of Diebold & Stoffa (1981). The seafloor appears in τ–p space (Figs 5b–9b) as a quarter ellipse with the lowest value of intercept time. Each reflection beneath the seafloor beings at $p = 0$ with an intercept time equal to the two-way travel time to that reflector, and intersects the path of the above reflector. These intersections comprise the

critical arrivals in the τ–p domain. The loci of the critical and post-critical arrivals in τ–p space form a continuous, monotonically decreasing function assuming that velocity does not decrease with depth. This high-amplitude trajectory contains all the information necessary to derive a velocity–depth function. Pre-critical reflection energy is located in the area

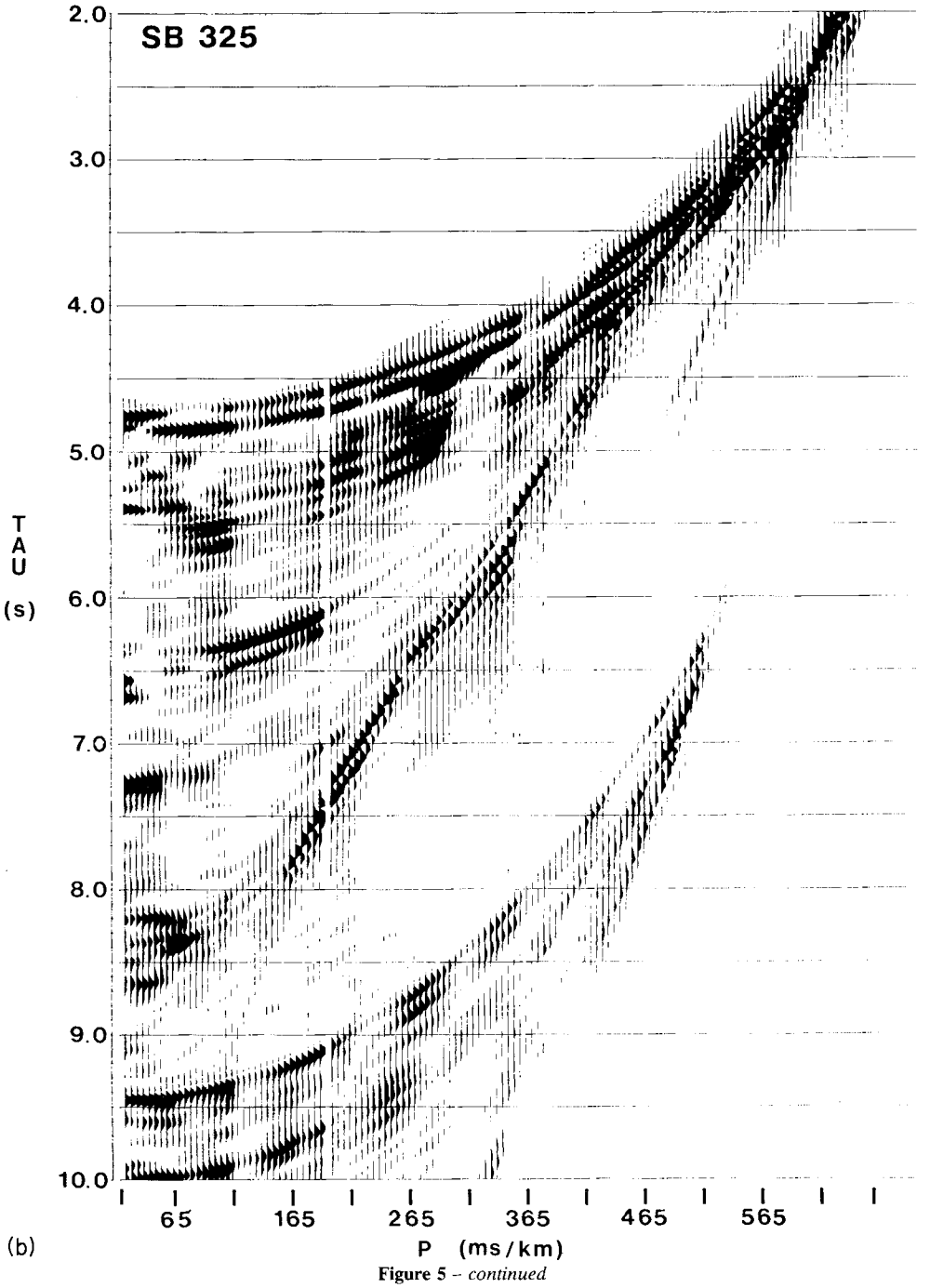

Figure 5 – *continued*

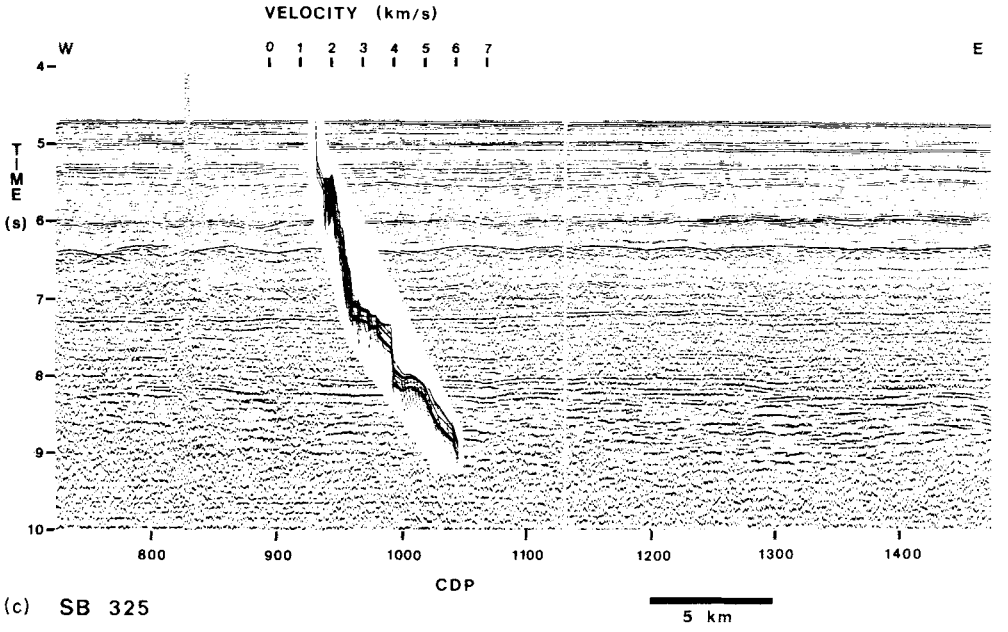

Figure 5 – *continued*

between the trajectory and the τ–p origin. Each ray parameter trace was Hilbert-transformed and bandpass-filtered, and the entire τ–p map was automatically scanned for maximum values of amplitude in order to define and subsequently derive an envelope for the path. The data utilized in the τ-sum inversion were chosen by determining the maximal data amplitudes in each filtered τ–p trace and recording the corresponding intercept times. Windowing in the

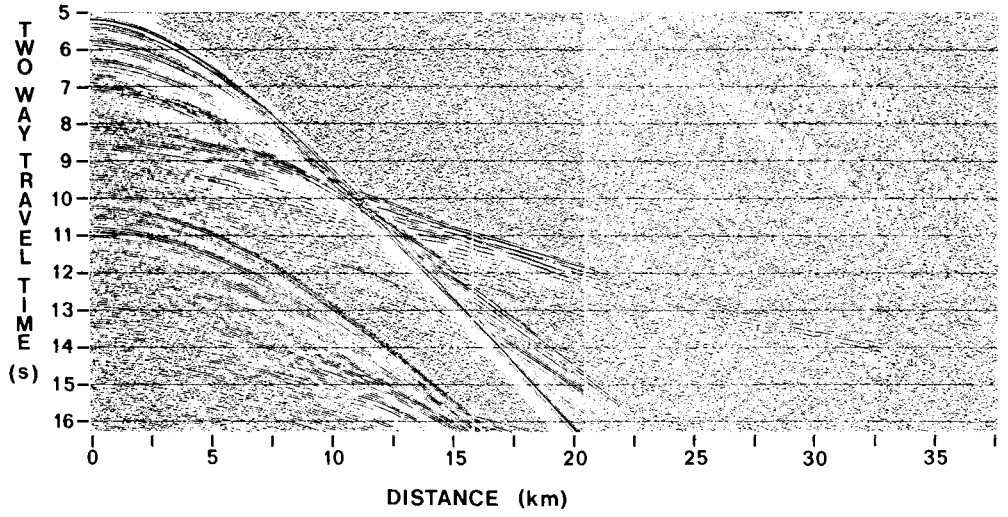

Figure 6. (a) The observational time–distance data for sonobuoy 350V36, with time-varying gain applied. (b) The τ–p map for sonobuoy 350V36. (c) The τ-sum inversion for sonobuoy 350V36 superimposed on coinciding multichannel seismic reflection profile 84V (Fig. 10).

τ–p plane helped exclude false data points, such as multiples and pre-critical reflections, and other dubious data were simply deleted. Confidence limits were placed on the data by assigning a τ-error, describing the uncertainty of any point on the τ-p map, and then computing the bounds by the method of Diebold *et al.* (1981). For each of the five sonobuoy data

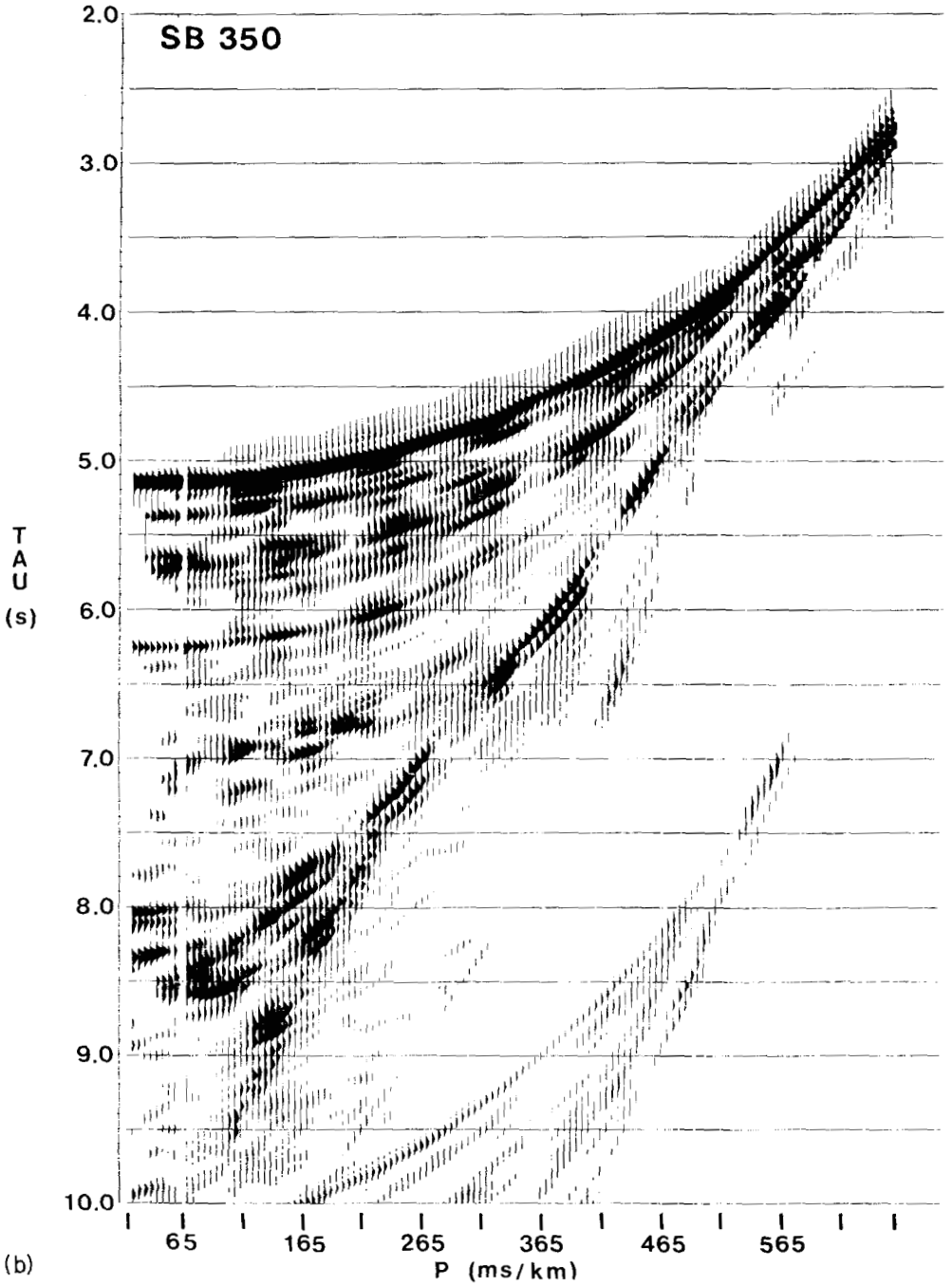

Figure 6 – *continued*

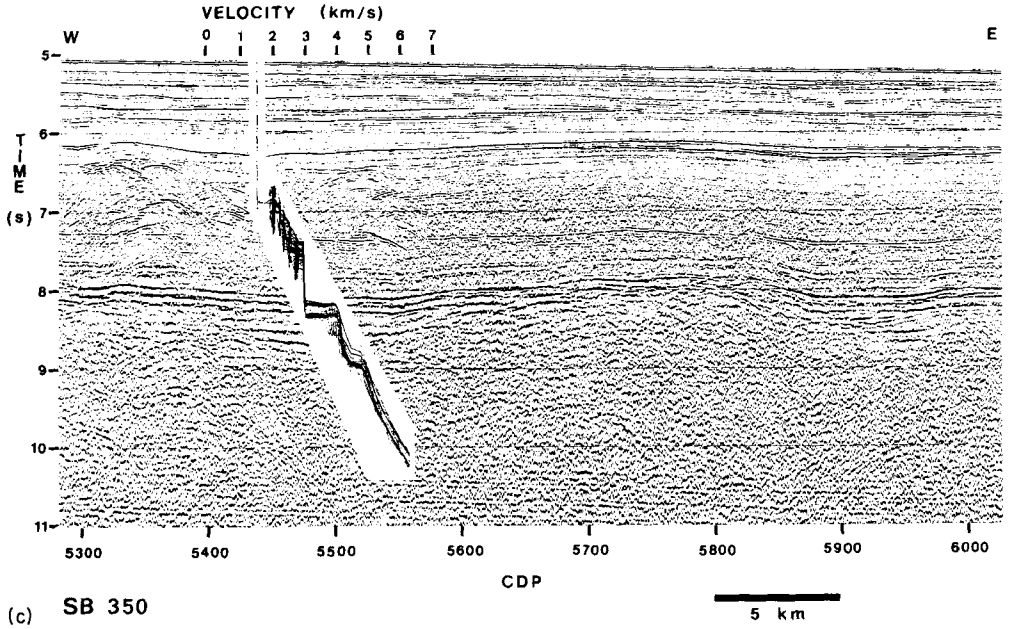

Figure 6 – *continued*

inversions a τ-error of 50 ms was employed (Mutter *et al.* 1984). Errors in p were not considered because of the dense sampling interval of p's and the relative insensitivity of the inversion method to ray parameters. The overall effects of the error-bounded inversion are to smooth the original velocity–depth step function, and falsely to enhance a more gradational

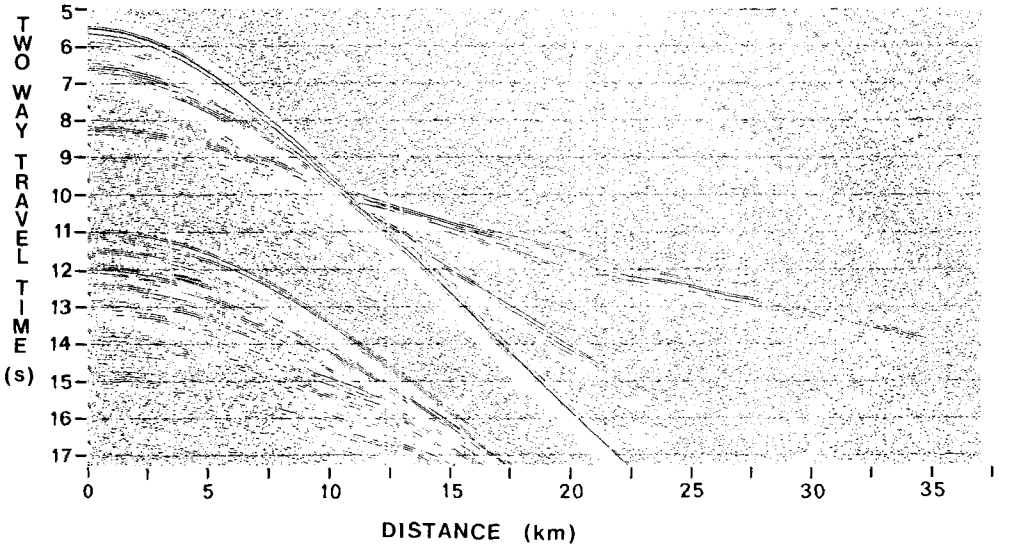

Figure 7. (a) The observational time–distance data for sonobuoy 354V36, with time-varying gain applied. (b) The τ–p map for sonobuoy 354V36. (c) The τ-sum inversion for sonobuoy 354V36 superimposed on coinciding multichannel seismic reflection profile 84V (Fig. 10).

velocity–depth function in deeper, faster layers as opposed to shallower, slower layers (Mutter *et al.* 1984). The bounds serve to indicate all conceivable 'worst-case' errors.

Examination of the τ–p extremal inversions (Figs 5c–9c) highlights the sensitivity of the inversion scheme to the proper choice of quarter-ellipses from the τ–p maps shown in

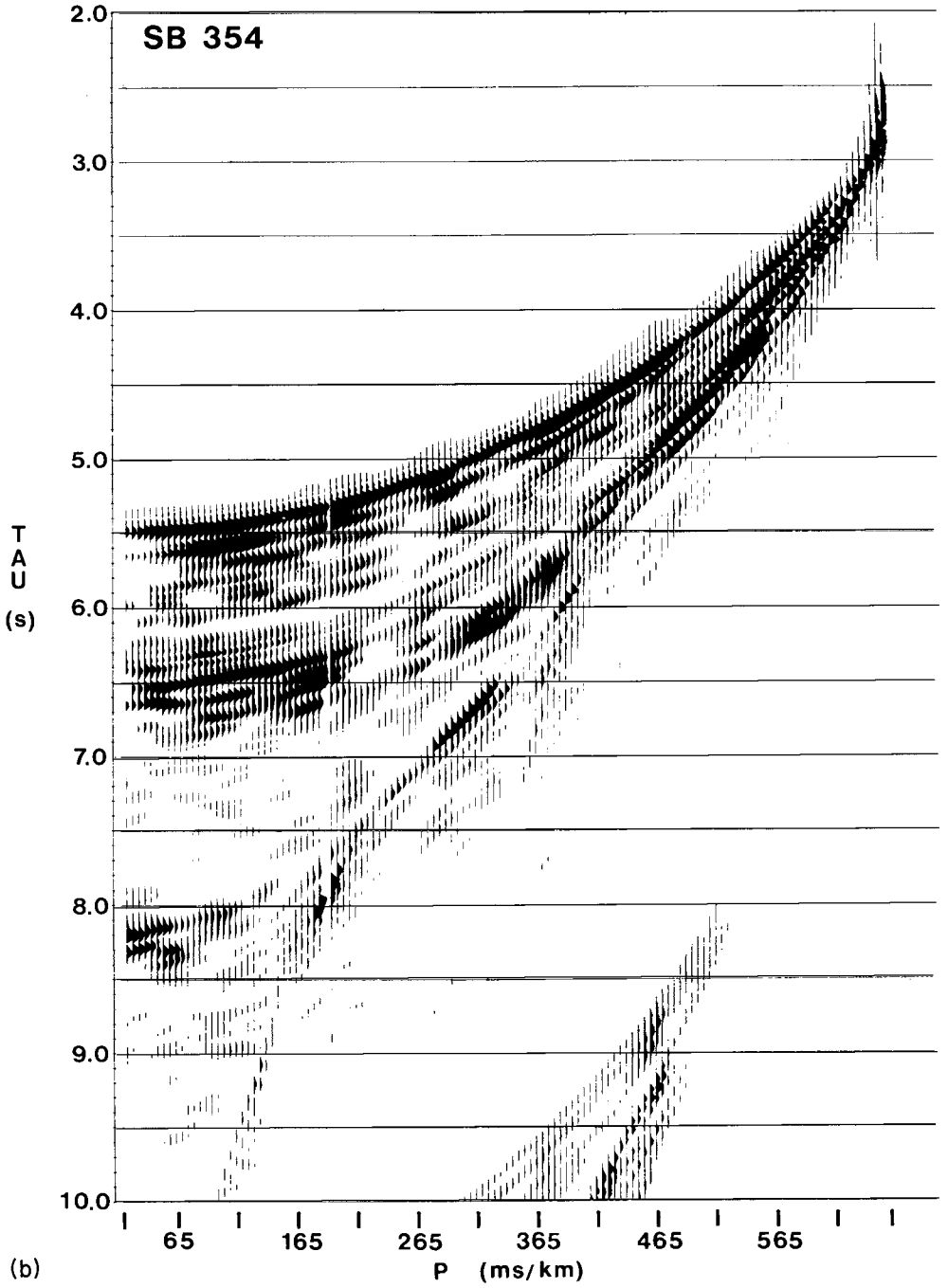

Figure 7 – *continued*

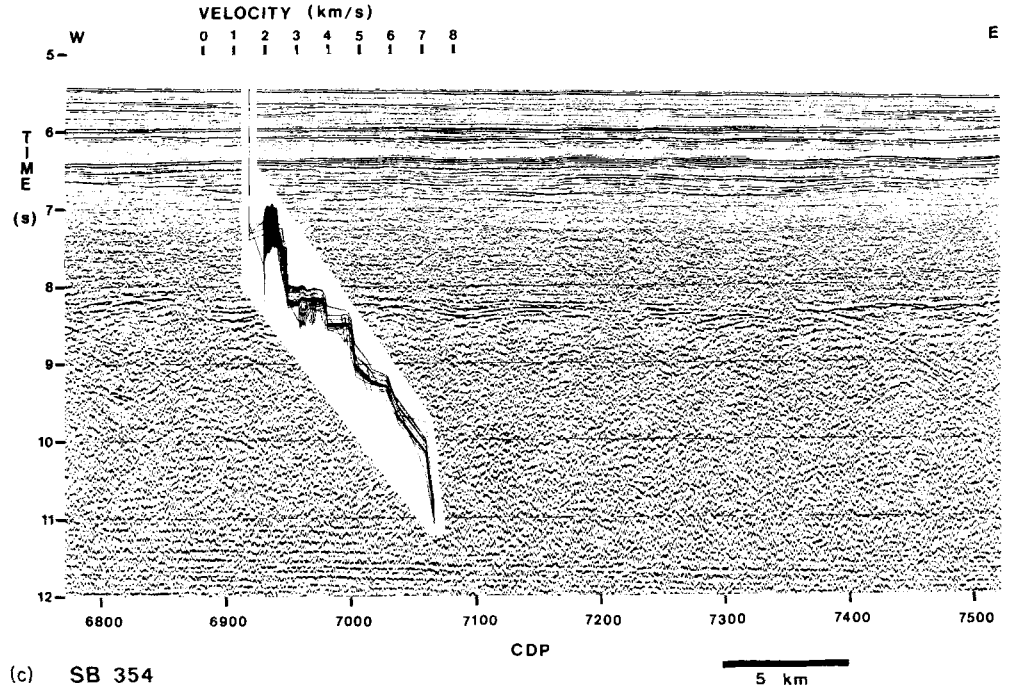

Figure 7 – *continued*

Figs 5(b)–9(b). The plethora of arrivals in the region of high ray parameters and low intercept times on the maps for all five sonobuoys (Figs 5b–9b) makes picking the proper trajectory there, either automatically or manually, extremely difficult. Stoffa *et al.* (1981) employed normal moveout corrections to provide information on the actual velocity structure in the

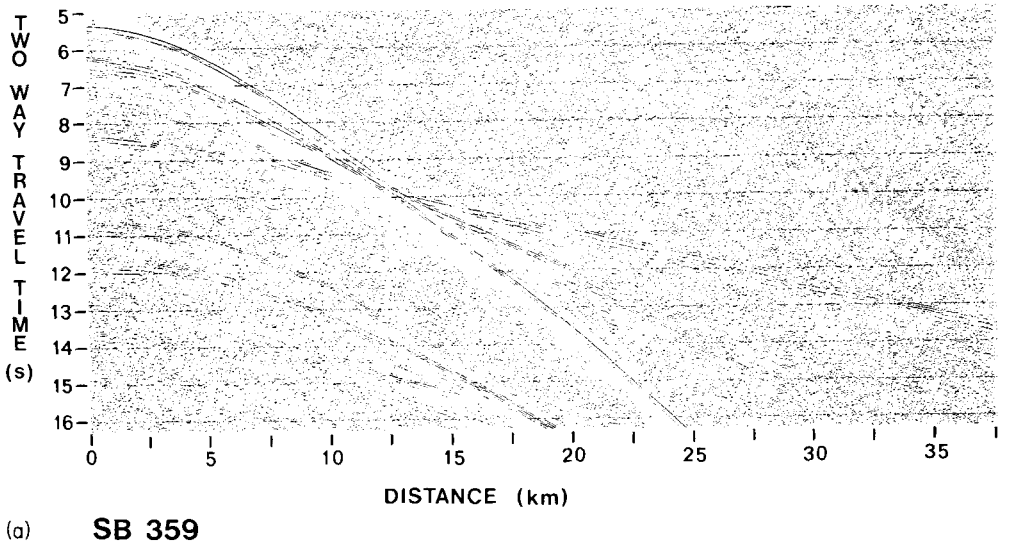

Figure 8. (a) The observational time–distance data for sonobuoy 359V36, with time-varying gain applied. (b) The τ–p map for sonobuoy 359V36. (c) The τ-sum inversion for sonobuoy 359V36 superimposed on coinciding multichannel seismic reflection profile 86V (Fig. 10).

upper sediment column. Because of our short seismic array length (1.2 km) and the significant water depths of the great majority of our experiments, we chose to rely instead on the T^2/X^2 results (Table 1) in defining the velocity structure of this part of the ocean crustal column. The T^2/X^2 results do not appear on the extremal inversions of Figs 5(c)–9(c);

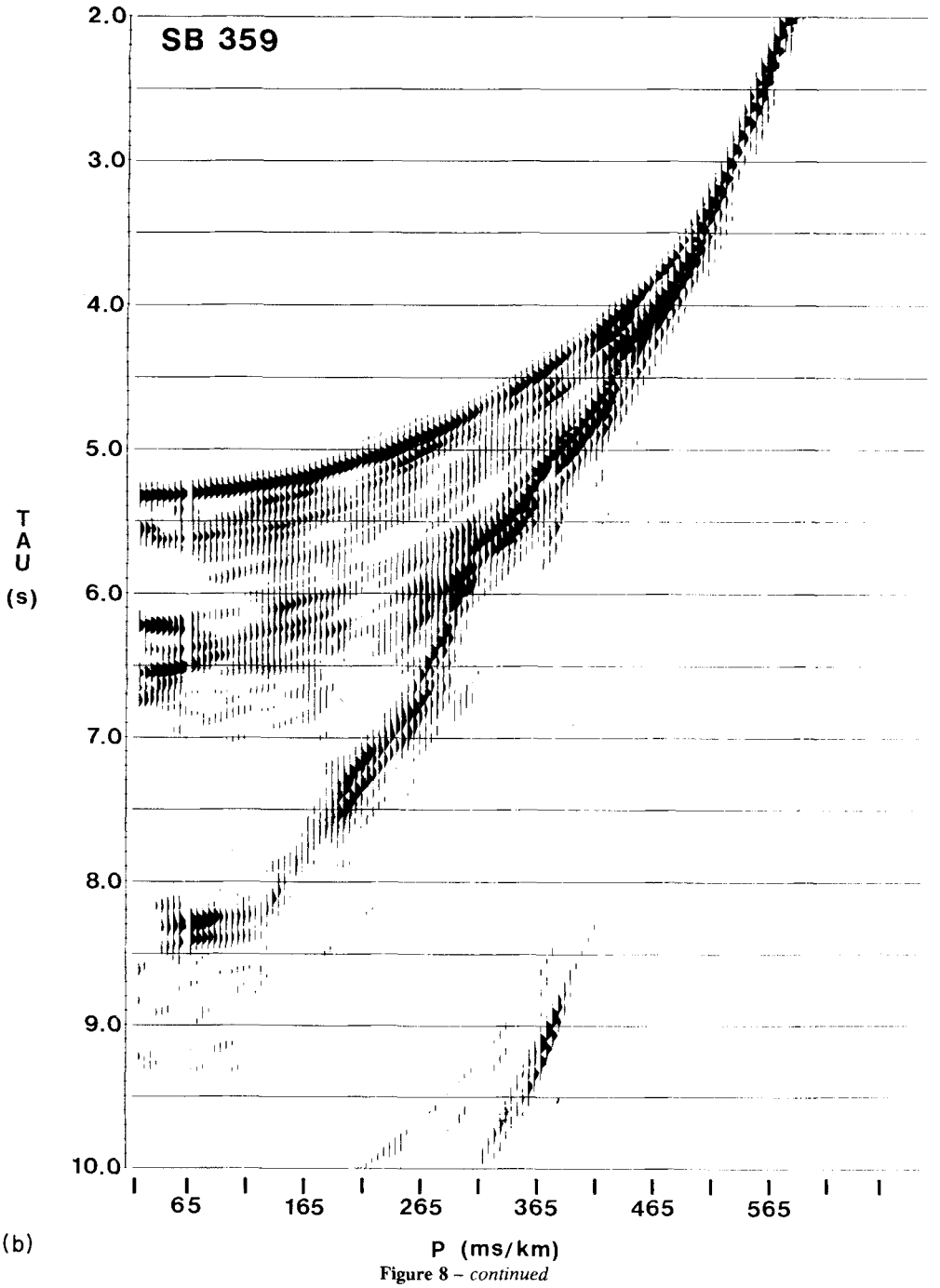

(b)

Figure 8 – *continued*

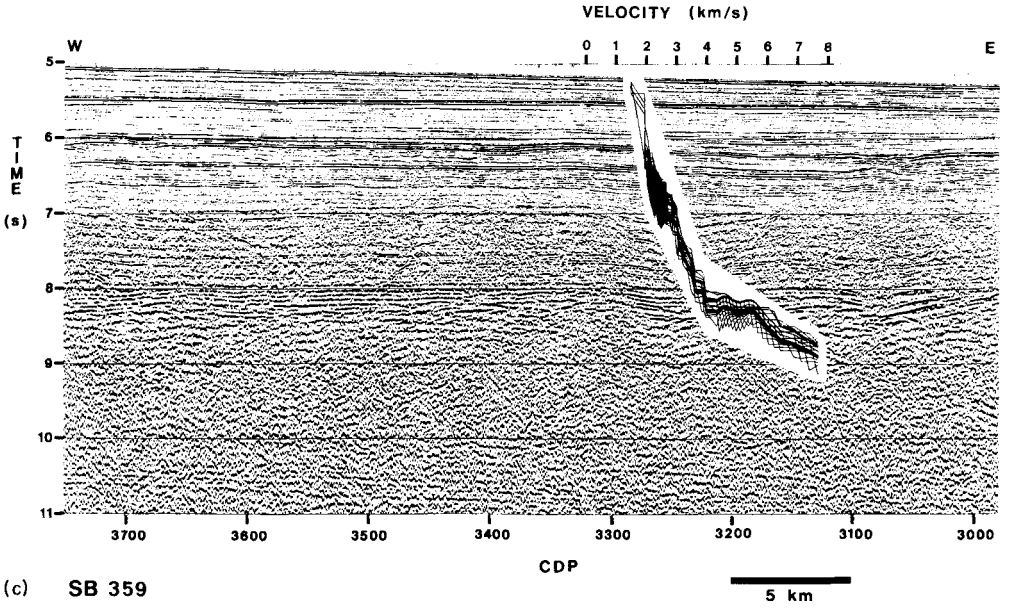

Figure 8 – *continued*

hence the straight lines emanating from the seafloor downward should be ignored until the extremal 'bounds' diverge.

Another problem encountered in τ–p mapping and τ-sum inversion occurs in the region of high intercept times and low ray parameters. Arrivals from deep layers (layer 3 and

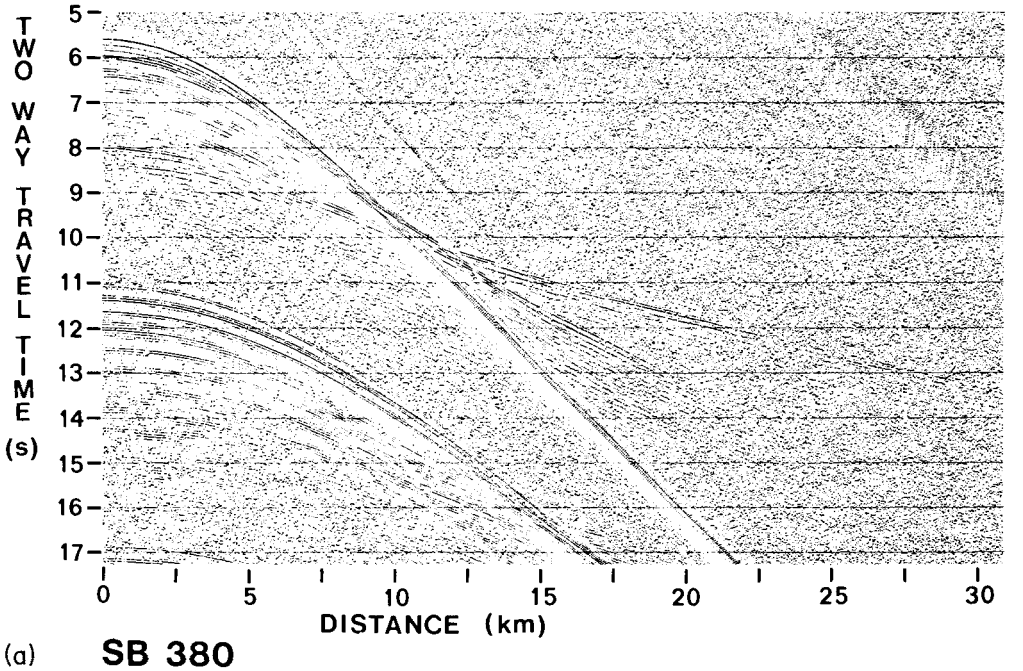

Figure 9. (a) The observational time–distance data for sonobuoy 380V36, with time-varying gain applied. (b) The τ–p for sonobuoy 380V36. (c) The τ-sum inversion for sonobuoy 380V36 superimposed on coinciding multichannel seismic reflection profile 90V (Fig. 10).

mantle) may not attain the post-critical range, and hence pre-critical reflections may dominate the τ–p map for this region. If the energy is misinterpreted as post-critical, the τ-sum inversion will create bogus high-velocity layers deep in the section. We have attempted to terminate each inversion before such ambiguity concerning the nature of the arrivals deep in the igneous crust arises. Caution must none the less be exercised in interpreting the deep segments of the τ–p inversions (Figs 5c–9c).

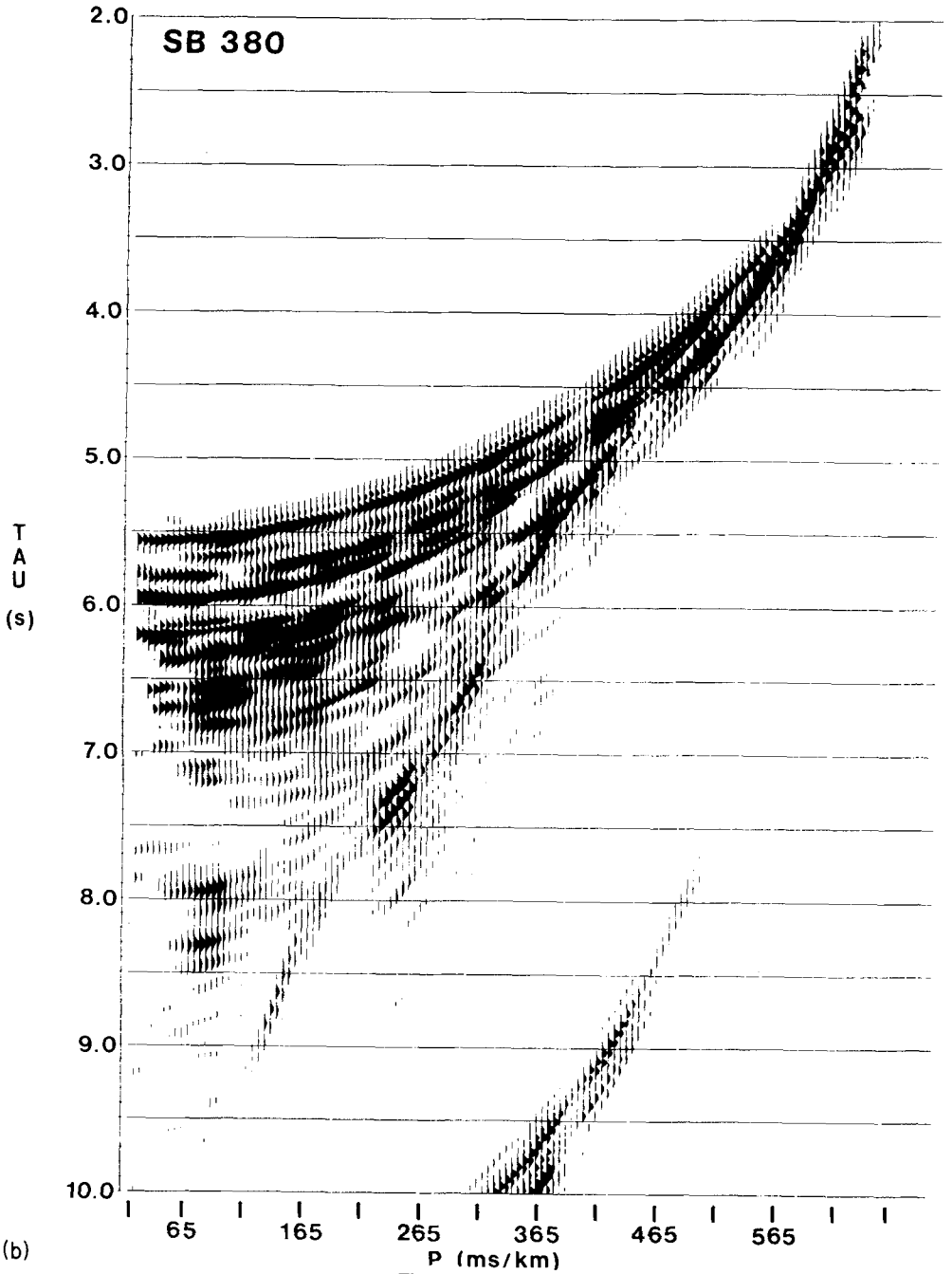

Figure 9 – *continued*

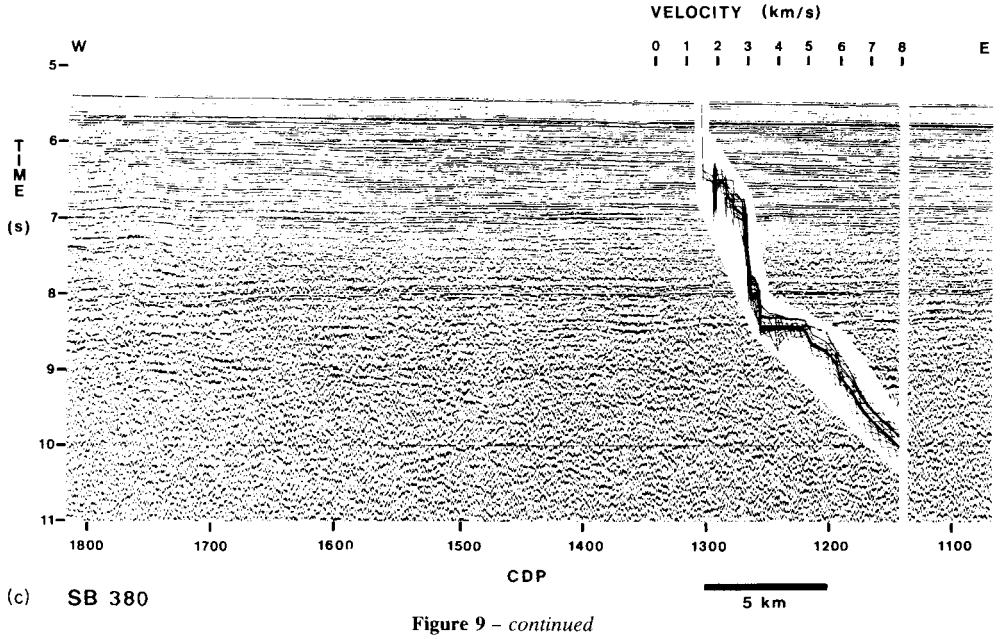

Figure 9 – *continued*

Crustal velocity structure

Velocities and layer thicknesses for the 126 Lamont–Doherty sonobuoy experiments plotted on Fig. 4 are listed in Table 1. The results from the other sonobuoy data sets (Francis *et al.* 1966; Lort *et al.* 1979), appear in Table 2 (see Fig. 4 for locations). In deriving a picture of the subseafloor velocity structure in the Comoros and Western Somali basins, we shall proceed from the seafloor through the sedimentary column and oceanic crust to mantle. All errors quoted are one standard deviation. Bear in mind that data abundance and resolution normally decrease with increasing depth.

SONIC VELOCITY IN SEDIMENTS: T^2/X^2 AND SLOPE–INTERCEPT RESULTS

Deep Sea Drilling Project Site 241, which penetrated 1174 m subbottom, was located at 4054 m water depth on the East African continental rise (Fig. 4) to establish a stratigraphic section (Simpson, Schlich *et al.*, 1974). Multichannel seismic lines 81V and 84V (Fig. 10) were run over the drillhole to aid in seismic stratigraphic correlations (Fig. 11). Sonobuoy experiments 332V36, 333V36, 335V36, 352V36 and 354V36 were performed over or near the drill site (Fig. 4) simultaneously with the multichannel seismic data acquisition. The average velocity structure derived from these five experiments, listed between the age/lithology section and multichannel seismic reflection record in Fig. 11, resulted in a reinterpretation of the leg 25 Initial Reports' correlation of reflectors with ages. In our interpretation the 'green' reflector is the Middle Eocene–Late Oligocene hiatus observed at ~ 470 m subbottom, and is the boundary between units I and II. Unit I is predominantly clay and clay-rich nannofossil oozes, and silty clays. Unit II differs slightly in lithology, being clay and silty clay claystones. Site 241 bottomed in silt-rich claystones of earliest Turonian age, and we do not believe the 'purple' reflector was penetrated. Proceeding downward in the section, the next prominent reflector is the 'red' horizon lying directly above the 'blue'

reflector (probable oceanic basement). Both deeper reflectors are marked compressional wave velocity discontinuities, and will be discussed later.

As part of seismic stratigraphy studies described elsewhere (Coffin & Rabinowitz 1986a) all available seismic reflection profiles in the study area (Fig. 1) were digitized for various reflectors (seafloor, green, purple, red, and blue in Fig. 11) down to the sediment–igneous crust interface employing the computer programs of Mountain (1981). To obtain true geological cross-sections, these digitized time sections had to be converted to depth sections through the application of velocity functions. Interval velocities determined by the T^2/X^2 technique from Tables 1 and 2 comprised the data base for deriving least-squares linear regressions and thus continuous velocity functions (Houtz 1974) of the form:

$$v = v_0 + Kt$$

where t is the one-way vertical travel time beneath seafloor in seconds. At time t, v is the 'instantaneous velocity', and the regressions are made on the midpoint (in time) of each layer. The intercept, v_0(km s^{-1}), is a statistical projection to the seafloor from data points beneath, and thus approximates the seafloor sound velocity. The slope, K (km s^{-2}), represents the acceleration of a vertically descending ray. Houtz (1974) chose to develop a continuous function instead of a step function based on the evidence that the velocity of sound generally increases smoothly with depth in marine sediments. Many measurements performed on Deep Sea Drilling Project cores corroborate that assumption. The form of the equation provides for easy integration to thickness as a function of reflection time, and higher-order polynomials do not significantly reduce the variance. To test reliability (scatter) and significance of the fit, respectively, standard errors and correlation coefficients were calculated for the regressions. Following careful examination of seismic reflection profiles for acoustic basement and subsequent editing of the sonobuoy results tabulated in Tables 1 and 2, we determined velocity functions for the two major basins in the study area, the Western Somali and the Comoros basins. Inspection of the data for geographical patterns and the subsequent derivation of statistically distinct velocity functions for the two basins justified the data division. In addition, a deep, high-velocity (4.58 ± 0.29 km s^{-1}) sediment layer is present in the Western Somali Basin. Such a layer cannot be positively identified in our limited data in the Comoros Basin. The boundary between the two velocity provinces is defined by the trend of the Comoros Islands, along approximately 12°S latitude (Fig. 1).

The velocity–time plots for the two basins appear in Figs 12 and 13. For the Western Somali Basin (Fig. 12) 346 layers were included in the regression. $V_0 = 1.577$, $K = 1.655$ km s^{-2} and the error on the computed value of V is ±0.280 km s^{-1}. The correlation coefficient, $R = 0.923$. The smaller Comoros Basin was the site of fewer sonobuoy experiments, and only 56 layers were used to derive a velocity function (Fig. 13). There, $V_0 = 1.637$, $K = 1.208$ km s^{-2}, and the error on V is ± 0.224 km s^{-1}. The correlation coefficient is 0.901. The values of V_0 and K for the two regressions fall in the middle of the ranges reported by Houtz (1974, 1977, 1980a,b, 1981) in other areas of the world. The correlation coefficients indicate (taking into account the number of points) that the lines are quite reliable, and the standard errors demonstrate limited scatter.

Two examples of the application of the derived velocity functions to digitized seismic reflection data (Mountain 1981) are the contour maps appearing in Figs 14 and 15. Both the total sediment thickness (Fig. 14) and depth to basement (Fig. 15) maps are contoured in kilometres, and seismic control is indicated by dotted lines. Although the detailed geological and geophysical implications of these maps are fully described elsewhere (Coffin & Rabinowitz 1986a,b) the major results may be summarized as follows. The total sediment thickness map records total sediment accumulations of 8+km adjacent to the continental margins of

Table 1. Sonobuoy solutions from the Somali and Comoros Basins.

Sonobuoy	Water Depth, m	Layer Thickness, km									‡ Mantle Reflection	Crustal Velocity,* km/s										Latitude, °N	Longitude, °E
		h_2	h_3	h_4	h_5	h_6	h_7	h_8	h_9	h_{10}		v_2	v_3	v_4	v_5	v_6	v_7	v_8	v_9	v_{10}	v_{11}		
322V36	3000	0.41	0.59	0.41	3.84	0.54	0.96	2.55				1.59*	2.17*	2.51*	3.73*	4.15	4.93	5.48	7.16			-3°31.2'	41°50.4'
323	3420	0.34	0.37	0.84	2.16	1.94	2.12	2.04	2.03		R	1.90*	2.03*	2.50*	3.00*	4.50*	5.50*	6.28	7.00	7.56		-3°24.6'	42°22.8'
324	3520	0.73	0.56	0.80	1.65	1.12	0.98	2.51				1.83*	2.45*	3.01*	3.03*	4.07*	4.35*	6.35	6.93			-3°21.6'	42°40.2'
325	3540	0.45	0.45	0.47	0.65	2.77	1.00	0.91	2.94		R	1.72*	2.18*	2.71*	2.95*	3.28*	5.26*	6.07	7.00	7.69		-3°18.0'	42°56.4'
327	3570	0.63	0.90	1.12	1.14	1.25	2.07	0.38	1.86		R	1.81*	2.08*	2.55*	3.80*	5.12*	5.34*	5.88	6.88	7.74		-3°13.2'	43°13.8'
328	3660	0.37	0.98	2.65	1.50	1.91	1.82				R	1.94*	2.23*	3.19*	4.83	6.08	6.75	7.51				-3°04.2'	43°28.8'
329	3690	0.36	1.24	1.50	1.01	1.00	1.28	1.18	2.41		R	1.81*	2.67*	2.80*	3.56*	4.76	5.68	6.54	7.40	8.06		-2°55.8'	43°43.8'
330	3800	0.42	0.50	0.95	1.45	0.53	0.38	0.95	1.21	2.73	R	1.97*	1.95*	2.80*	3.50*	4.27*	4.48	5.28	6.06	6.50	7.55	-2°45.0'	44°01.8'
332	3950	0.46	0.41	0.52	2.08	0.59	1.56	1.67				1.97*	2.03*	2.66*	2.85*	(4.5)	5.49	6.20	6.84			-2°31.8'	44°22.8'
333	4040	0.76	0.43	0.57	0.92	1.25	1.04	1.06	2.56		R	1.81*	2.35*	2.61	2.89	4.56	5.45	6.22	6.73	7.63		-2°20.4'	44°40.8'
335	4160	0.55	0.66	0.56	2.67	1.24	1.76	3.42			R	1.95*	2.07*	2.42*	3.54*	5.40	6.51	7.12	7.70			-2°07.2'	45°01.2'
336	4250	0.42	0.33	0.95	2.00	1.04	0.94	1.28	1.02	1.82	R	1.67*	2.28*	2.80*	3.23*	4.72*	5.52	6.42	6.96	7.44	8.52	-1°55.2'	45°17.4'
339	3750	0.60	0.68									1.85*	2.67									-0°56.4'	44°52.2'
340	2740	0.49	0.41	1.28	0.54	1.31	1.64					1.86*	2.10*	2.48*	2.79*	3.85	4.25	5.04				-0°17.4'	43°33.0'
341	250	0.19	0.31	0.41								1.81	2.07	2.25	2.44							-0°18.6'	42°48.0'
342	720	0.59	0.31	0.43	0.74	0.26	0.76	0.99	2.28			1.87	2.14	2.38	2.61	2.77	3.05	3.26	3.62	4.36		-0°51.6'	42°58.2'
344	510	0.38	0.22	0.47								(1.8)	2.01	2.46	2.82							-0°58.8'	42°18.0'
347	2740	0.49	0.43	0.71	1.90	0.15						2.01*	2.20*	2.67*	2.84	3.04	3.48					-1°25.2'	42°51.6'
348	3460	0.54	0.80	1.14	1.05	1.59	0.79	0.79	0.96	1.33		1.86*	2.71*	2.85*	3.14*	4.13*	4.40*	(4.8)	5.35	6.03	6.65	-1°55.2'	43°25.8'
349	3560	0.43	0.57	0.94	1.10	1.36	1.06	1.29	1.06	3.47	R	1.55*	2.26*	2.56*	2.94*	4.25*	4.95	6.01	6.81	7.30	8.10	-2°00.6'	43°42.0'
350	3830	0.60	0.50	0.90	2.05	0.89	1.24	1.26	2.92		R	1.61*	2.27*	2.39*	3.83*	4.68	5.40	5.88	6.64	7.52		-2°06.0'	44°15.0'
352	4040	0.50	0.40	0.60	1.44	1.01	1.17					1.85*	1.81*	2.34*	2.94*	4.58*	5.46*					-2°20.4'	44°39.0'
354	4100	0.44	0.44	0.40	1.45	0.87	0.88	0.66	0.94	2.69	R	1.74*	1.94*	2.23*	2.99*	4.06*	4.91	5.70	6.49	7.16	7.82	-2°27.0'	44°45.0'
355	4560	0.74	1.02	0.88	0.53	0.97	1.82					1.71*	2.44*	3.08*	4.38	5.13	5.68	6.22				-2°39.4'	45°47.4'
356	4650	0.59	0.40	0.48	2.14	0.87	0.91					1.92*	2.08*	2.85*	(3.5)	4.98	5.84	7.01				-3°23.4'	45°51.0'
358	4240	0.43	0.78	0.89	0.97	0.73						1.78*	2.30*	2.51*	3.51*	4.72*						-3°24.0'	44°33.0'
359	3980	0.87	0.64	1.70	0.69	0.72	1.97	2.55			R	1.84*	2.43*	2.95	4.44	5.30	6.37	6.98	7.55			-3°16.2'	44°07.8'
360	3500	0.75	0.63	0.67	2.89	1.78						2.09*	2.35*	2.53*	3.53*	5.84*						-2°57.6'	43°00.6'
361	3360	0.43	1.17	0.70	3.19							1.64*	2.34*	3.16*	3.71*	4.37						-2°49.2'	42°42.6'
362	3290	1.07	0.68	0.72	1.24	0.53	0.85	0.38				(2.0)	2.47	2.88	3.19	3.96	4.46	4.80	6.47			-2°44.4'	42°33.6'
365	2860	1.29	0.21	0.63	0.64	1.05	1.96					(2.2)	2.61	2.92	3.27	3.62	3.99	4.38				-2°31.2'	42°03.6'
366	2350	0.47	0.80	0.99	0.97							(1.8)	2.24	2.99	3.42	3.95						-2°25.8'	41°39.6'
367	90	0.15	0.19	0.28	0.34							(1.8)	2.35	2.99	3.59	4.00						-2°27.6'	40°58.8'
368	160	0.17	0.23	0.41	0.70							2.21	2.89	3.39	3.80	4.19						-2°40.2'	40°45.0'
372	290	0.29	0.21	0.51	0.48							1.90	2.82	3.39	4.00	4.92						-2°56.4'	40°56.0'
373	360	0.77	0.47									2.03	2.42	3.18								-3°10.8'	40°30.6'
374	720	0.61	0.27	0.39	0.50	0.59	0.36					1.98	2.23	2.49	2.87	3.30	3.82	4.25				-3°15.0'	40°49.2'
375	1650	1.63	1.96	0.14	1.70							2.15*	2.99*	3.55	4.78	5.28						-3°22.2'	41°08.4'
376	2970	0.47	1.39	1.41	1.01	1.21	1.38	2.61				2.03*	2.51*	2.62*	3.60*	4.75*	5.42*	5.80	6.59			-3°31.8'	41°49.2'
377	3620	0.55	0.45	0.73	1.70	0.82	0.42	1.10	1.77			1.96*	2.18*	2.64*	2.63*	4.02*	4.40	5.36	6.12	7.05		-3°52.2'	42°41.4'
378	4110	0.32	0.30	1.04	0.92	0.78	1.23					1.58*	1.74*	2.34*	3.48*	3.47*	4.63	5.98				-4°09.6'	43°31.8'
379	4330	0.69	0.37	0.40	0.45	1.12	0.92	0.98	3.05			1.88*	1.86*	2.31*	2.88*	3.79*	4.83	5.78	6.36	7.13		-4°14.4'	44°02.4'
380	4150	0.47	1.06	1.62	0.86						R	1.86*	2.40*	2.97*	4.51*	(5.0)	5.40	6.00	6.65	7.20	7.65	-5°10.2'	43°34.8'
381	3930	1.23	0.35	0.48	1.83	0.19	1.33	0.59	1.43	1.96	R	2.07*	2.49*	3.18*	3.52*	4.27*	4.85	5.17	5.94	7.40	8.20	-5°04.2'	43°01.2'
382	3560	0.41	0.39	0.51	0.80	0.91	0.82	2.07	1.24			1.66*	2.24*	2.41*	3.27*	3.15*	3.92*	4.94*	5.77*			-4°55.2'	42°27.0'
383	3190	0.32	0.47	0.51	1.36	0.69	1.29					1.64*	2.20*	2.51*	3.10	3.47	3.96	4.51	5.71			-4°43.2'	41°57.6'
384	2780	0.61	1.07	1.24	1.40	1.70	1.87					2.10*	2.57*	3.06*	4.01*	5.30*	5.42	6.13				-4°27.6'	41°36.0'
385	1540	0.38	0.36	0.89	0.52	0.42	1.12	0.76				1.71*	2.25*	2.57*	(2.8)	3.01	3.87	4.36	4.74			-4°08.4'	41°01.8'
386	1210	0.61	0.69	0.57	0.63	0.73	0.80					1.99*	2.51*	2.46*	3.40*	3.49*	4.35	4.66				-4°01.2'	40°43.2'
387	970	0.83	0.29	0.47	0.42	0.79						1.98	2.38	2.76	3.22	3.87	4.29					-3°58.2'	40°24.0'
388	890	0.59	0.53	0.86								1.83*	2.26*	2.98*								-3°55.8'	40°16.2'
389	340	0.13	0.43	0.48	0.81	0.74						1.89	1.98	2.38	2.89	3.59	3.97					-3°59.4'	39°50.4'
390	510	0.66	0.18	0.35	0.82							1.86	2.19	2.60	2.94	3.31						-4°19.2'	39°46.2'
391	710	0.48	0.19									1.90	2.04	2.59								-4°28.8'	39°57.0'
392	1050	1.59	1.76									2.23*	3.75*	3.62								-4°40.2'	40°08.4'
393	1550	0.44	0.49	0.61	1.03	2.07	1.76					1.88*	2.08*	2.54*	3.13*	3.66*	5.17*					-4°51.6'	40°21.0'
394	2000	0.35	0.47	0.53	0.86	0.65	1.74					1.57*	2.28*	2.63*	2.76*	3.70*	4.20*					-5°00.0'	40°43.2'
396	2560	0.60	0.32	0.52	0.51	1.14	1.04	1.03	1.40			1.88*	2.00*	2.55*	2.75*	2.72*	4.01*	4.78	5.40	6.21		-5°15.6'	41°13.2'
397	2930	0.38	0.53	0.69	0.79	0.86	0.79					1.81*	2.01*	2.65*	3.42*	3.37*	3.86*	4.38				-5°24.6'	41°28.8'
398	3060	0.86	0.49	0.56	0.67	1.80	0.86	1.38	1.20	3.02	R	1.89*	2.56*	2.71*	2.81*	4.01*	5.38*	5.62	6.46	7.18	7.72	-5°29.4'	41°57.2'
399	3430	0.44	0.48	0.72	0.85	2.41	1.32	3.05				1.60*	1.96*	2.87*	2.99*	4.27*	5.86	6.77	7.29			-5°46.8'	42°07.8'
400	3680	0.63	0.42	0.52	0.97	1.32	1.39					1.81*	2.04*	2.61*	3.36*	3.95	4.72	5.46				-5°59.4'	42°26.4'
401	3800	0.59	0.47	0.41	0.90	0.66						1.86*	2.42*	2.47*	2.90*	3.15*						-6°26.4'	42°49.2'

402	3570	0.48	0.46	1.15	0.84	3.03	0.16					1.90*	2.08*	3.14*	3.37*	4.81*	5.48	6.42				-6°33.0'	42°25.2'
403	3170	0.43	0.41	1.07	0.61	1.30	1.78	1.60				1.82*	2.15*	2.38*	3.40*	4.06*	(4.5)	5.71	6.19			-6°43.2'	41°48.6'
404	2870	0.52	0.50	0.57	0.61	1.28	1.61	1.71	0.89			1.84*	2.45*	2.47*	2.97*	3.72*	4.02*	4.88*	6.17			-6°47.4'	41°30.0'
405	2630	0.57	0.53	0.82	1.58	0.31	1.02	2.02	1.88	7.76	R	2.02*	2.40*	2.73	3.33	4.07	4.76	5.53	6.38	7.22	8.52	-6°51.0'	41°11.4'
406	1760	0.57	0.60	0.70	2.91	0.59	2.05					1.73*	2.24*	2.78*	3.56*	4.39	4.93	6.02				-6°55.8'	40°32.4'
407	720	0.50	0.31	0.39	0.46	0.73	0.98	0.73	1.15			(1.8)	2.17	2.51	2.86	3.16	3.64	4.59	5.02	5.70		-7°01.2'	40°05.4'
408	660	0.32	0.36	0.43	0.35	0.31	0.56	0.75	0.64	0.68		(1.7)	1.94	2.23	2.59	2.92	3.18	3.50	3.90	4.14	4.62	-7°19.2'	39°59.4'
411	1340	0.36	0.51	0.51	0.69	1.19	2.33	1.62				1.59*	2.25*	2.51*	3.07*	3.85*	4.27	5.06	5.61			-7°29.4'	40°13.8'
412	790	0.41	0.18	0.32	0.29	0.42	0.68	0.63	0.73			(1.8)	1.96	2.27	2.50	2.87	3.18	3.48	3.97	4.46		-8°01.8'	39°57.0'
413	1400	0.37	0.39	0.82	2.03	0.73						1.66*	2.20*	2.45*	2.94	3.86	4.73					-8°11.4'	40°11.4'
414	2530	0.62	0.65	1.79	1.22	1.34	1.93	1.39				1.94*	2.55*	2.69*	4.06*	4.98*	5.52*	5.78	6.44			-8°04.8'	40°48.6'
415	2920	0.66	0.67	0.46	1.01	0.95	2.43					2.01*	2.45*	2.85*	2.93*	3.06*	4.95*					-8°04.2'	41°18.6'
416	3010	0.46	0.61	0.52	0.90	1.35	1.19	1.09	1.15	1.84		1.75*	2.56*	2.66*	2.69*	3.64*	4.58	4.96	5.60	6.35	6.74	-8°04.2'	41°26.4'
417	3360	0.72	1.24	0.60	0.96	0.40	0.94					2.06*	2.51*	2.77*	(3.5)	3.99	4.68	5.21				-8°03.6'	41°55.8'
418	3680	0.45	0.53	0.71	0.91	1.37	1.95	1.09				1.74*	2.26*	2.73*	3.25*	3.86*	4.64	5.74	6.31			-8°01.8'	42°30.6'
420	3890	0.58	0.41	0.49	0.82	1.58	0.74	2.29	1.69			2.05*	2.04*	2.17*	3.34*	4.40*	5.70	6.46	7.21	8.07		-8°01.2'	43°04.8'
421	4000	0.78	0.80	1.33								(1.8)	2.28	3.37	5.07							-8°20.4'	43°26.4'
422	3570	0.33	0.43	0.66	0.81	0.44	0.53	1.81				1.62*	2.20*	2.50*	3.01*	(3.5)	3.95	4.32	6.07			-9°00.6'	42°47.4'
423	3520	0.48	0.68	0.82	0.72							2.10*	2.50*	3.08*	3.44*							-9°01.2'	42°25.8'
424	3160	0.67	0.54	0.82	0.77	0.94	0.76	1.41	2.02		R	1.98*	2.21*	3.15*	(3.5)	3.91	4.45	5.13	5.95	6.99	7.96	-9°04.2'	41°55.8'
425	3070	0.64	0.86	1.07	1.24	0.24	0.95	1.51	1.60			1.79*	2.82*	3.11*	(3.5)	4.01	4.63	5.12	5.73	6.19		-9°05.4'	41°12.6'
426	2580	1.36	0.75	0.54	0.50							(2.2)	2.83	3.18	3.44	4.11						-9°09.2'	40°29.0'
427	2540	0.46	1.09	1.33	0.94	0.83	0.59	1.66	1.05			1.67*	2.91*	3.03*	4.09*	(4.5)	4.74	5.55	6.15	6.84		-9°09.0'	40°04.2'
428	1720	0.75	0.81	1.62	0.36	2.95						1.84	2.48	2.98	4.04	4.76	5.38					-8°37.2'	39°58.8'
430	1840	0.55	0.47	0.91	0.78	1.05	1.16	1.18				1.76*	2.12*	2.59*	2.79*	3.89	4.39	5.13	5.75			-5°45.6'	40°23.4'
431	2080	0.47	0.44	0.89	1.28	0.26	0.55	0.84	0.65			1.84*	2.04*	2.79*	(3.0)	3.25	3.56	4.21	4.79	5.30		-5°47.4'	40°36.0'
432	2660	0.45	0.41	0.94	0.69	0.58	0.84					1.60*	2.05*	2.65*	(2.8)	3.08	3.57	4.18				-5°51.6'	41°06.0'
433	3340	0.48	0.62	0.53	0.81							1.86*	2.21*	2.70*	3.17*							-6°05.4'	41°59.4'
434	3510	0.64	0.45	0.59	1.96	1.04	0.53					1.66*	2.08*	2.70*	(3.5)	4.42	5.30	6.34				-6°11.4'	42°17.4'
435	3790	0.41	0.41	0.59	1.58	1.41						1.99*	1.91*	2.83*	2.95*	4.42	5.51					-6°19.8'	42°43.8'
436	3990	0.56	0.37	0.52	0.46	0.56						1.79*	2.18*	2.47*	2.69*	2.88*						-6°29.4'	43°16.2'
437	3840	1.08	0.52									2.05*	2.35*									-9°36.0'	44°42.6'
438	4220	0.33	0.33	0.54	0.54	1.49	0.60	1.58				1.52*	1.97*	2.14*	2.61*	3.38	4.25	5.44	6.49			-3°39.0'	44°13.2'
439	3730	0.80	0.45	0.60	1.87	1.98	1.09					1.56*	2.06*	2.59*	2.54*	3.93*	3.90*					0°46.2'	46°24.6'
440	4810	0.40	0.39	0.76	0.86							1.57*	1.85*	2.33*	3.49*							-1°30.6'	47°55.8'
441	4790	0.41	0.36	1.26								1.81*	2.28*	3.16*								-5°28.8'	47°56.4'
442	4780	0.67	0.86									1.90*	2.88*									-5°37.2'	47°57.6'
444	4510	0.58	0.68	0.69	0.74							1.83*	2.72*	2.77*	3.71*							-9°19.2'	47°15.6'
445	4740	0.35	0.81	0.89	0.40							1.91*	2.07*	2.71*	(4.0)	5.4						-3°27.6'	46°08.4'
447	3740	0.43	0.45	0.72	0.52							1.63*	2.07*	2.89*	3.18*							-10°28.2'	45°25.2'
448	3630	0.48	0.39	0.66								1.73*	1.98*	2.82*								-10°38.4'	45°25.2'
449	3490	0.38	0.43	1.20	0.66	0.78	0.24	0.25	1.09	2.17		1.62*	2.37*	2.48*	2.80*	2.82*	3.38	3.81	5.30	6.12	7.08	-13°30.0'	45°53.4'
450	3360	0.35	0.78									1.62*	2.16*									-14°10.2'	45°45.0'
451	3300	0.36	0.43	0.99	1.58	1.20						1.64*	1.85*	2.54*	3.22*	3.54*						-14°21.6'	45°43.2'
452	3260	0.93	0.68	0.52	1.32							1.84*	2.47*	2.49*	2.67*							-14°31.8'	45°40.8'
453	3130	0.48	0.62	0.64	1.16	0.81						1.79*	2.34*	2.36*	2.42*	3.23*						-14°42.6'	45°37.8'
455	2440	0.94	2.44									1.86*	2.65*									-15°12.0'	45°36.0'
456	2350	1.97										2.13*										-15°27.6'	45°27.0'
457	3160	0.71	0.91	0.89								1.74*	1.93*	2.88*								-15°15.6'	45°04.2'
458	3290	0.79	0.65	0.73								1.71*	2.22*	2.97*								-15°10.2'	45°01.8'
459	3410	0.37	0.55	0.59	1.79	2.02						1.70*	2.32*	2.51*	3.40*	(3.6)	3.96					-14°58.2'	44°56.4'
460	3460	0.31	0.59	0.77	1.38							1.61*	2.23*	2.40*	2.91*							-14°46.2'	44°51.6'
461	3530	0.66	0.40	0.55	0.71	0.87	1.32					1.51*	2.13*	2.70*	2.88*	3.04*	4.54*					-14°08.4'	44°40.2'
462	3540	0.80	0.92	0.95	0.82	1.73						1.82*	2.59*	3.13*	3.33*	4.61*						-13°54.8'	44°32.4'
464	3260	0.45	0.77									1.70*	2.44*									-15°42.6'	43°27.6'
249C12	2770	0.91	1.18									1.88*	2.49*									-14°25.7'	41°13.3'
250	2870	0.35	0.83	0.51	0.84							1.86*	2.04*	2.31*	3.04	4.61						-13°14.0'	41°51.4'
251	2440	0.57	0.66									2.11*	2.55*									-12°27.5'	41°05.0'
252	3390	0.52	0.47	0.71	2.43	1.04						1.52*	2.61*	2.85*	3.63*	4.34*						-9°25.0'	42°45.5'
253	3880	0.38	0.29	0.35								1.51*	2.03*	2.30*								-8°58.2'	43°49.7'
254	4280	1.36										2.78*										-7°55.9'	45°19.0'
255	5030	1.18										2.19*										-3°05.6'	50°13.6'
256	5040	0.34	0.30	0.33	0.47							1.94*	2.08*	2.33*	(3.0)	5.96						-2°39.4'	50°19.3'

* Interval velocity.

† Values in parentheses are assumed velocities (for refractions or over observed reflection intervals).

‡ R indicates mantle solution reconciled to multichannel mantle reflections.

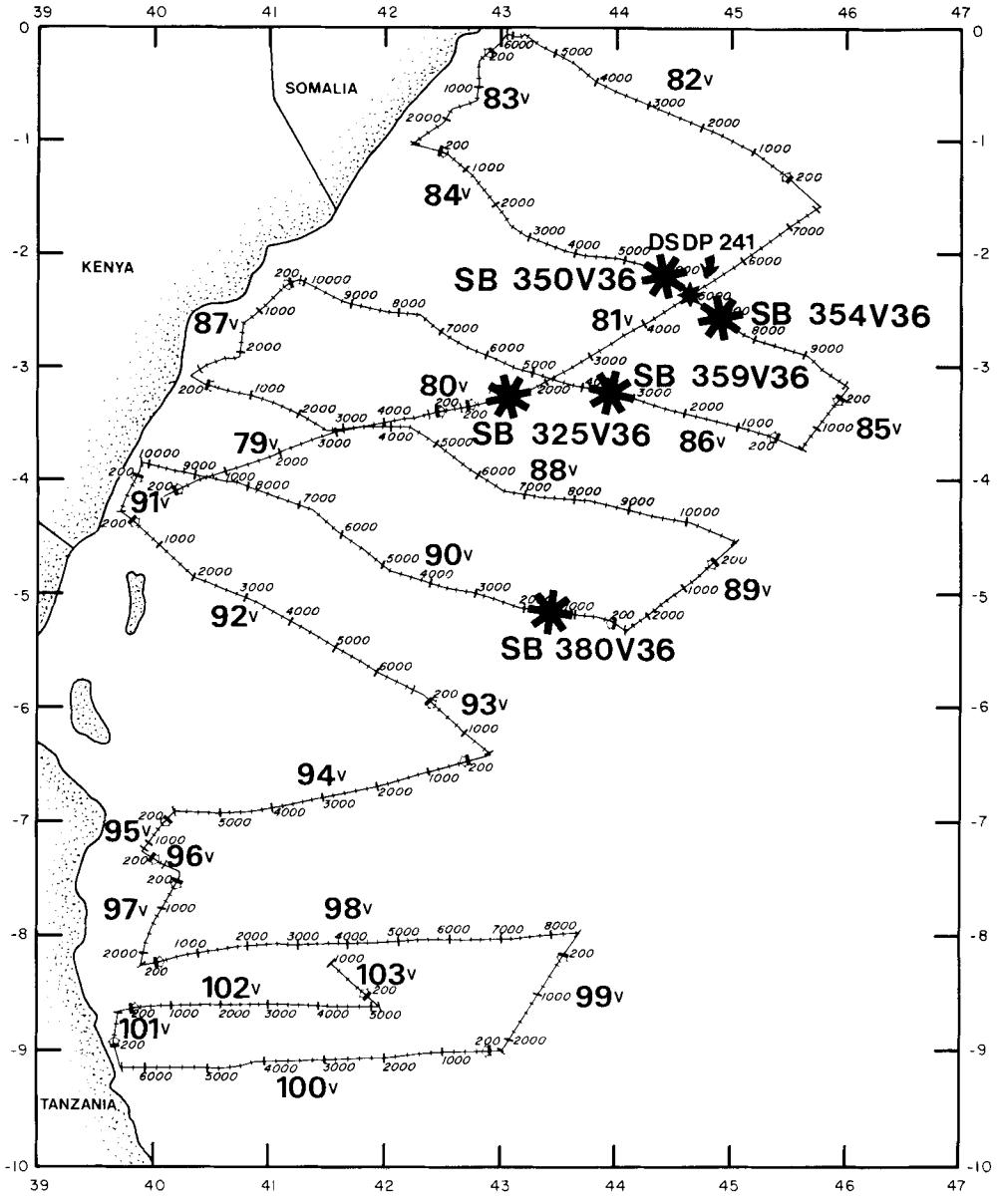

Figure 10. Locations of sonobuoys chosen for $\tau-p$ analysis and CDP navigation for coinciding multichannel seismic reflection data.

Somalia, Kenya and Tanzania, and thicknesses of 5+km on the insular margin of northern Madagascar. Maximum sediment thicknesses for both the East African and Madagascar margins are probably greater than the two figures given above, but acoustic basement was impossible to discern when sediment thicknesses exceeded those numbers on the respective margins. Notable sediment accumulations also occur in the moat of the Wilkes Rise, in the Amirante Trough, along the Davie Fracture Zone, and along the Chain Ridge (see Fig. 1 for location of these features). The depth to basement map illustrates the tectonic regimes and

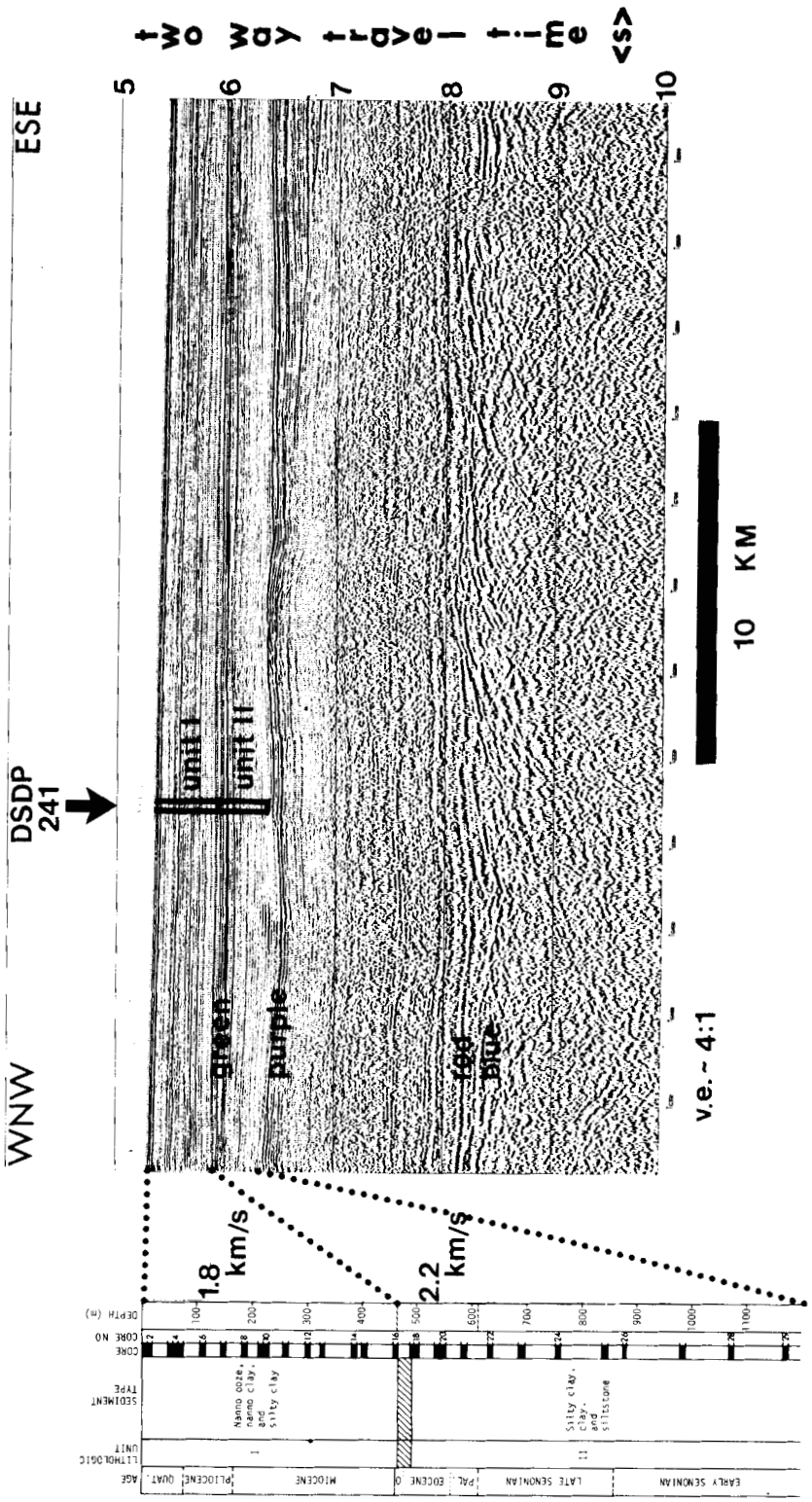

Figure 11. Correlation of multichannel seismic reflection line 84V (Fig. 10) with the results of DSDP site 241 (after Coffin & Rabinowitz 1982).

Table 2. Sonobuoy solutions of Francis *et al.* (1966) and Lort *et al.* (1979).

Refraction Station	Water Depth, m	Layer Thickness, km				Crustal Velocity,† km/s					Latitude, °N	Longitude, °E
		h_2	h_3	h_4	h_5	v_2	v_3	v_4	v_5	v_6		
FDH00	1460	1.0	3.4	9.3		(1.7)	2.88	4.71	7.04		-2°23'	41°22'
FDH00	1460	1.0	2.3	1.5	9.0	(1.7)	2.88	3.49	4.71	7.04	-2°23'	41°22'
FDH01	2060	1.4	3.1	8.1	4.0	(1.7)	3.54	4.80	7.16[1]	(8.1)	-1°45'	42°07'
FDH02	3600	0.9	2.6	3.1	3.3	(1.8)	2.52	5.28	7.00[1]	8.08	-2°40'	43°28'
FDH03	4170	1.0	2.7	4.6		1.93	2.53	6.56	8.14		-2°31'	44°56'
FDH04	4810	0.7	1.0	2.5	5.9	1.79	2.49	5.28	6.85	(8.1) 8.54[1]	-2°55'	47°02'
FDH05	5040	0.1	0.6	3.5 2.5		1.91	(2.5)[1] 2.63[1]	4.20	7.88		-3°28'	49°36'
FDH06	5060	0.3	3.1			(1.8)	6.24	8.18			-3°36'	51°29'
L6	2870	1.20	1.32			2.12*	3.14*				-15°40'	42°06'
L7	3560	0.54	0.39	1.61		1.80*	2.32*	2.92*			-14°21'	44°21'
L8	3520	0.75	0.94	0.51	1.84	1.90*	2.22*	3.16*	3.40*	5.6	-13°57'	45°15'
L9	3320	0.36	0.61	0.44	0.58	1.80*	2.34*	2.75*	3.40*	4.1	-15°21'	43°09'

★ Interval velocity.
† Values in parentheses are assumed refraction velocities.
[1] Velocity from a single run.

structural complexity of the study area (Fig. 15). The N–S trending Davie Fracture Zone dominates the western portion of the map. In the southern half of the central part of the map, the Wilkes Rise, Cosmoledo Group and Comoros Islands are distinctive. The eastern third of the map is quite complex. Proceeding from north to south, the Chain Ridge, trending NE–SW, merges into the roughly N–S trending basement lineaments of Bunce & Molnar (1977). To the south and east are the western edge of the Seychelles Bank and the

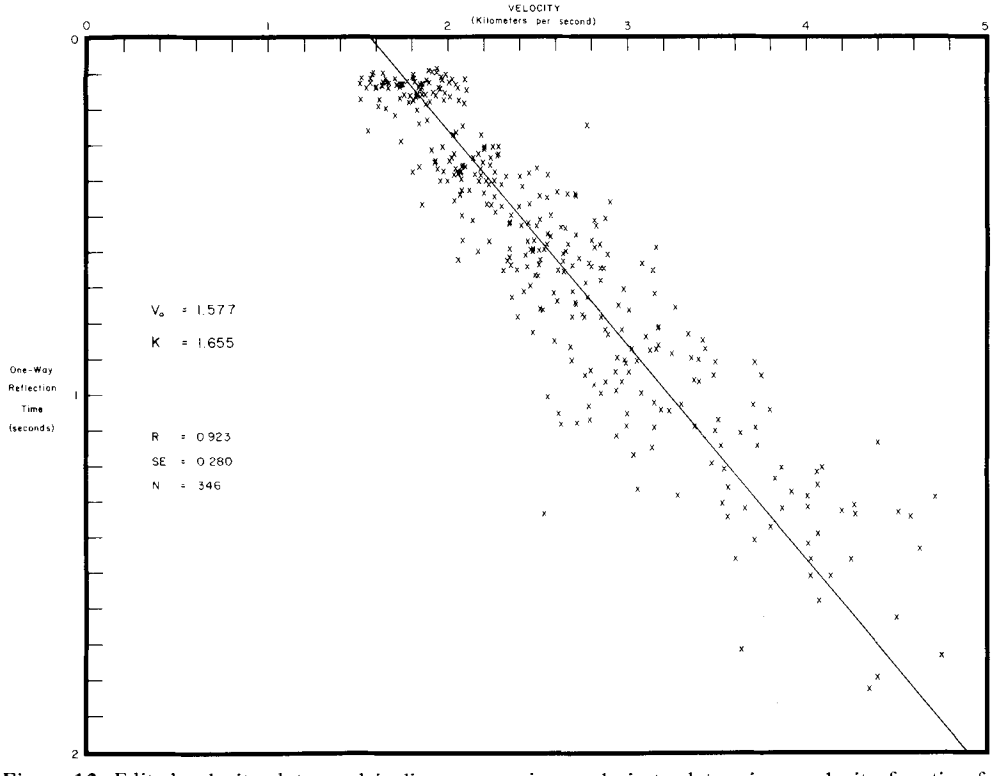

Figure 12. Edited velocity data used in linear regression analysis to determine a velocity function for sediments of the Western Somali Basin.

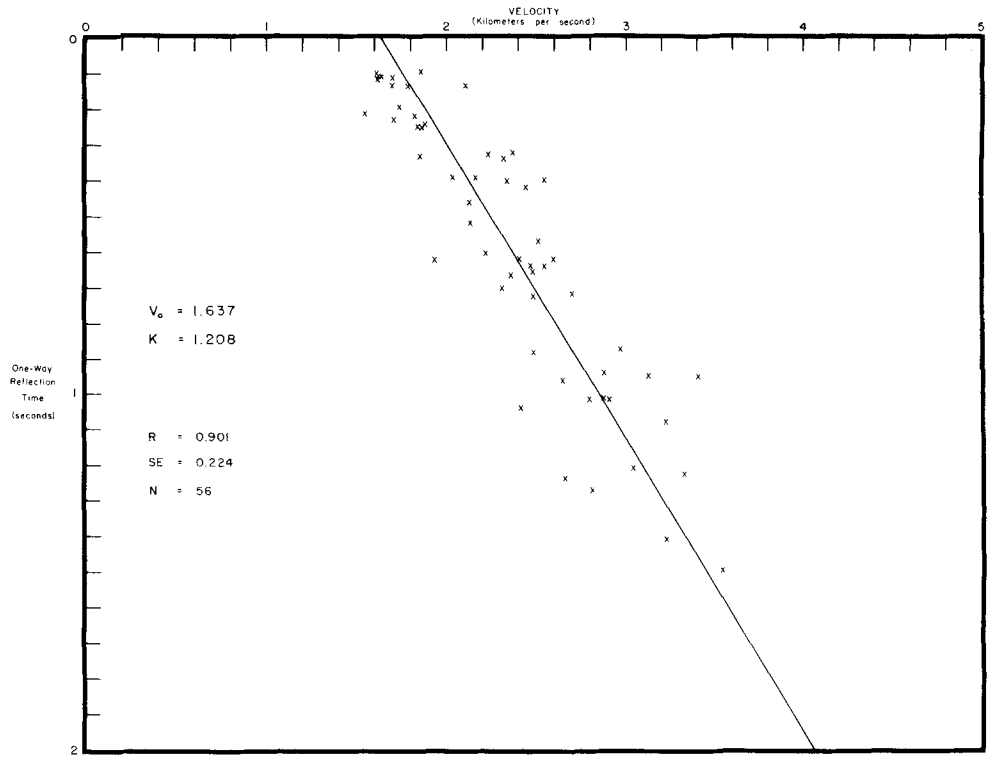

Figure 13. Edited velocity data used in linear regression analysis to determine a velocity function for sediments of the Comoros Basin.

Amirante Ridge and Trough system. Just to the NE of the northern tip of Madagascar are the islands of the Farquhar Group (see Fig. 1 for location of all of the preceding features).

A salient feature in the velocity structure of the crust of the Western Somali Basin (and possibly of the Comoros Basin) is a deep, high-velocity sediment layer overlying oceanic basement. The upper surface of this layer corresponds to the 'red' reflector in Fig. 11, a prominent horizon on much of the multichannel seismic reflection data acquired near the East African continental margin (Fig. 10). The reflector may be present elsewhere in the study area (Fig. 1), but it can only be positively identified (with two possible exceptions in the Comoros Basin) on our multichannel data, which are limited to the lines shown in Fig. 10.

Forty-seven of the sonobuoy experiments utilizing two 7.6 litre airguns as the energy source detected the high-velocity sediment layer either by the T^2/X^2 method (21 cases) or the conventional slope-intercept technique (26 cases). Our criteria for identifying the layer in these 47 instances were quite stringent. First, all buoys for which dip appeared significant, usually greater than 5°, were eliminated. Then the buoys for which the T^2/X^2 or slope-intercept results for both the high-velocity sediment layer and acoustic (igneous) basement could not be correlated with coincident or nearby seismic reflection profiles were deleted. The velocity of the layer ranges from 4.01 to 5.38 km s^{-1}, and the mean velocity obtained from 47 detections is 4.58 ± 0.29 km s^{-1}. The calculated thickness of the layer ranges from ~ 200 m (lower limit of resolution) to 3000 m. We shall further discuss the high-velocity sediment layer when describing the results of the five sonobuoys selected for τ–p mapping and inversion.

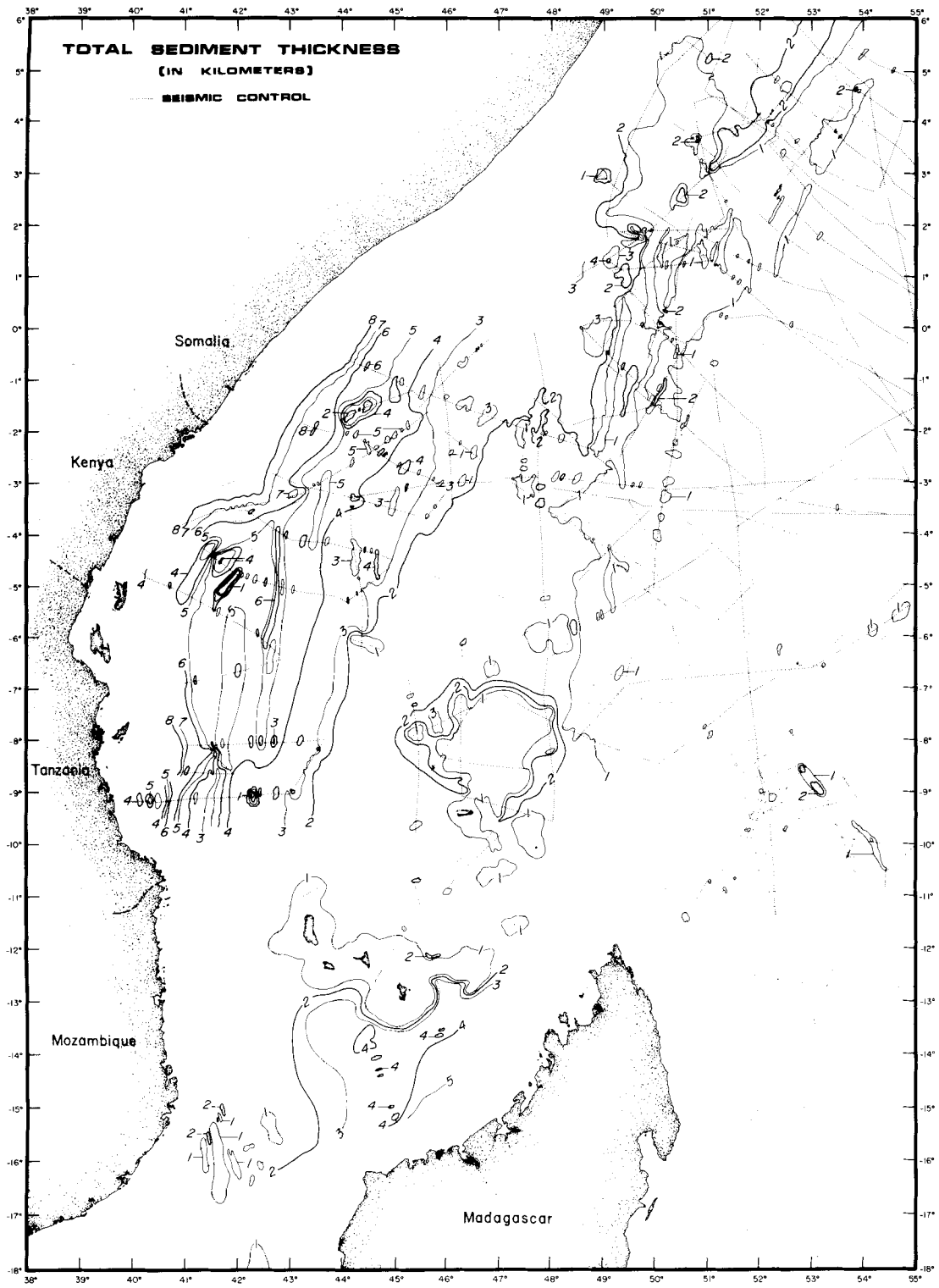

Figure 14. Total sediment thickness map of the study area compiled and contoured from digitized seismic reflection data (Mountain 1981) though application of the velocity functions described in the text.

Figure 15. Depth to basement map of the study area compiled and contoured from digitized seismic reflection data (Mountain 1981) through application of the velocity functions described in the text.

SONIC VELOCITY IN OCEANIC BASEMENT: SLOPE–INTERCEPT AND T^2/X^2 RESULTS

Of 107 sonobuoy experiments (Table 1) employing large-volume airguns conducted during the R/V *Vema* cruises in the study area (Fig. 4), 48 detected arrivals from the top of oceanic basement unambiguously, 42 by the conventional slope-intercept method and six by the T^2/X^2 technique. The criteria for choosing the data were: (1) lack of significant dip, and (2) correlation of layer velocities and depths with the rough, hyperbolated package of reflectors on multichannel seismic data usually associated with the top of oceanic basement. The velocity for the top of acoustic basement varies from 4.51 to 6.35 km s^{-1} in the 48 cases, and the mean is 5.40 ± 0.37 km s^{-1}. The orientations of our sonobuoy experiments were generally either parallel or perpendicular to the East African continental margin and roughly perpendicular to the Madagascar insular margin, and the strike of these margins varies. Hence the experiments (Fig. 4) were essentially randomly orientated with respect to the tectonic fabric of the study area as described by Rabinowitz *et al.* (1983) and Coffin & Rabinowitz (1986b). We tested for correlations between azimuth and velocity in our analyses of oceanic basement velocity structure, and none were apparent.

Differentiation of seismic layers 2 and 3 proved possible on the basis of the sonobuoy results listed in Table 1. Combined T^2/X^2 and slope-intercept methods applied to 27 sonobuoys define layer 2 as 2.73 ± 0.84 km thick with a mean velocity of 5.83 ± 0.27 km s^{-1}. Velocities within layer 2 range from 4.83 to 6.54 km s^{-1}, and up to three T^2/X^2 interval velocities and/or slope-intercept refractions are observed within it. Two-thirds, or 18 of 27 conventional slope-intercept solutions show layer 2 to be composed of two distinct velocity layers, possibly correlative with layers 2b and 2c. The mean velocity of the upper layer is 5.42 ± 0.19 km s^{-1}, with values ranging from 4.98 to 5.70 km s^{-1}. Its thickness varies from 0.72 to 2.12 km, with a mean of 1.22 ± 0.39 km. The lower layer has a mean velocity of 6.23 ± 0.22 km s^{-1}, with a range of values from 5.84 to 6.54 km s^{-1}. The mean thickness is 1.54 ± 0.47 km, varying from 0.91 to 2.29 km. We tested for systematic variations in the thicknesses of layers 2, 2b and 2c relative to distance from the East African continental margin, and no correlations were forthcoming.

Seismic layer 3 was detected in 19 sonobuoy experiments, 16 of which permitted the determination of layer thicknesses. The velocity of layer 3 was defined by a single refraction in all but three cases in which two refractions were observed. The velocity ranges from 6.50 to 7.44 km s^{-1} with a mean of 7.03 ± 0.25 km s^{-1}. The mean thickness of layer 3 is 2.62 ± 0.71 km, with values varying from 1.69 to 4.53 km and no apparent correlation between thickness and velocity. Again no correlation was apparent between layer 3 thickness and distance from the margin.

A total of 16 sonobuoy experiments enabled us to calculate the thickness of the entire igneous oceanic crustal column as well as integrated sea-surface to mantle crustal thickness. The mean thickness of layer 2 plus layer 3 is 5.22 ± 0.64 km, with values ranging from 3.73 to 6.42 km. In terms of two-way travel time, the thickness varied from 1.17 to 2.00 s, with a mean of 1.62 ± 0.22 s for the 16 experiments. Forward modelling via ray tracing using the combined T^2/X^2 and slope-intercept velocity solutions allowed us to corroborate these determinations of total igneous crustal thicknesses. A map of the study area with plotted values of total crustal thickness derived from our experiments and those of Francis (1964) and Francis *et al.* (1966) appears in Fig. 16. Sonobuoy 405V36, showing a depth to mantle of 19.1 km, is to be regarded as suspect; the experiment was performed in the vicinity of the Davie Fracture Zone (Fig. 3), and an extremely thick (7.76 km) layer 3 was determined. We observed a general trend of decreasing crustal thickness away from the East African continental margin, especially east of 49°E where the two experiments FDH05 and FDH06 exhibiting extremely shallow mantle are located.

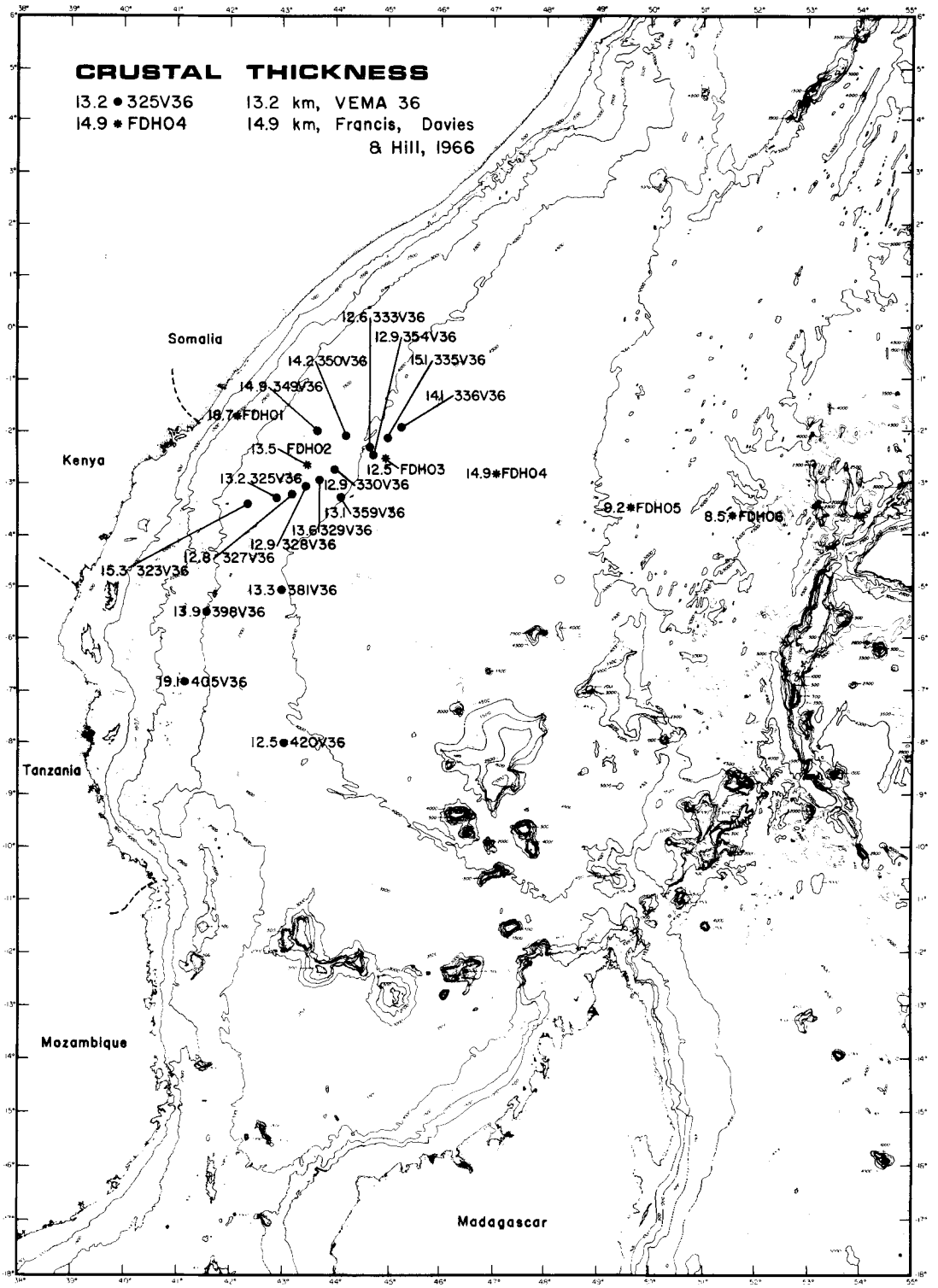

Figure 16. Crustal thicknesses (sea surface to mantle) determined from this study and that of Francis *et al.* (1966).

Finally, 19 of our sonobuoy experiments displayed mantle arrivals with velocities ranging from 7.51 to 8.52 km s^{-1}. The mean velocity for the top of the mantle is 7.85 ± 0.32 km s^{-1}, and there appears to be no correlation of experiment azimuth with velocity. No correlation is apparent between layer 3 thickness and mantle velocity.

SONIC VELOCITY IN DEEP SEDIMENTS AND OCEANIC BASEMENT: τ–p RESULTS

Five sonobuoys were selected for τ–p mapping (Stoffa *et al.* 1981) and τ-sum inversion (Diebold & Stoffa 1981) to resolve the velocity structure better in the deep sediments and igneous crust of the Western Somali Basin. All five buoys (Fig. 10) were deployed during multichannel seismic leg 18 of R/V *Vema* cruise 36 over the lower continental rise offshore East Africa. Water depths varied from 3500 to 4200 m for the experiments. For each buoy we have plotted the original X–T data (Figs 5a–9a), their maps in τ–p space (Figs 5b–9b), and the τ-sum inversions superimposed on coinciding multichannel seismic reflection profiles (Figs 5c–9c).

The general characteristics of the X–T data for each of the five sonobuoys (Figs 5a–9a) are quite similar. All show numerous wide-angle reflection and refraction arrivals to ranges exceeding 35 km. The critical distances for first arrivals of refracted mantle energy lie between 28 and 35 km, and the five buoys all display strong first arrivals in this range. Only two buoys, 325V36 (Fig. 5a) and 380V36 (Fig. 9a), show strong D-waves; for the other three buoys we assumed a constant shot spacing of 50 m. Forward modelling of the seafloor reflection subsequently confirmed this approximation.

Sonobuoy 325V36 (Fig. 5a) was deployed on seismic strike line 81V (Fig. 10) over presumed Jurassic Magnetic Quiet Zone crust. The strike of the seismic line is roughly parallel to the Mesozoic magnetic anomalies identified farther to the east by Rabinowitz *et al.* (1983). The τ–p map of the data (Fig. 5b) shows a well-defined band of energy at τ's ranging from 4.5 to 8.0 s. At intercept times greater than ~ 8.0 s, the amplitudes of the arrivals are severely diminished, and the inversion was terminated at $p = 165$ ms km^{-1}. This ray parameter corresponds to a velocity of 6.0 km s^{-1}, and probably lies somewhere within seismic layer 2. A strong converted shear arrival appears as a coherent branch emanating from the primary energy trajectory at an intercept time of approximately 2.8 s. One other sonobuoy, 350V36, also displays shear energy in the τ–p domain (Fig. 6b). In neither case were the shear arrivals employed in the τ-sum inversions. Pronounced ringing due to bubble pulse and/or internal multiples is observed in post-critical arrivals between τ's of 5.5 and 8.0 s, and is most severe between 5.5 and 6.5 s. This is a troublesome characteristic inherent in the other four τ–p maps as well (Figs 6b–9b), and attempts to deconvolve the data prior to τ–p mapping did not rectify the problem. The ringing significantly complicates identifying the true primary energy trajectory of critical and post-critical arrivals, and thus may result in inaccurate velocity determinations if incorrect arrivals are picked and employed in the τ-sum inversion procedure. As mentioned previously, errors in p are not considered in the τ-error determination and subsequent τ-sum extremal inversions described by Diebold *et al.* (1981) and applied to our five sonobuoy data sets. Hence the 'bounds' displayed in the five τ-sum inversions (Figs 5c–9c) do not account for possible false ray parameter picks resulting from ringing. The interface between sediments and oceanic basement appears in the τ–p map (Fig. 5b) as a break in slope of the trajectory at τ–p coordinates of (7.5 s, 185 ms km^{-1}).

The τ-sum inversion of sonobuoy 325V36 (Fig. 5c) data depicts velocity gradually increasing in sediments to a depth of 7.2 s, where it increases dramatically to a value between 4.0 and 4.3 km s^{-1}. Because of double high-amplitude peaks in this section of the τ–p map

(Fig. 5b) due to ringing, better velocity resolution as well as positive correlation with the 'red' reflector of Fig. 11 are not possible. A layer characterized by this velocity range extends to approximately 8.1 s two-way travel time, where the top of oceanic basement (the 'blue' reflector of Fig. 11) is indicated by a sudden increase in velocity to ~ 5.0 km s^{-1}. Velocity then increases gradually to a value of 6.0 km s^{-1} at 9.1 s two-way travel time where the inversion was terminated.

Two sonobuoy experiments, 350V36 and 354V36, were performed over Jurassic Magnetic Quiet Zone age crust flanking DSDP Site 241 (Fig. 4). The buoys were deployed along multichannel seismic dip line 84V (Fig. 10) (Coffin & Rabinowitz 1982, 1983) at an acute angle to the trend of magnetic anomalies further to the east. The τ–p map of 350V36 data (Fig. 6b) shows a fairly continuous band of energy between τ's of 3.0 and 9.5 s. At intercept times greater than 8.0 s, it proves extremely difficult to differentiate between pre- and post-critical reflection energy. We did, however, choose a trajectory in this region and terminated the inversion at $p = 160$ ms km^{-1}, corresponding to a velocity of 6.3 km s^{-1}. Between τ's of 5.7 and 6.8 s, a shear arrival appears as an isolated quarter-ellipse. Marked ringing is observed between intercept times of 5.8 and 7.5 s, again enhancing the possibility of choosing an energy trajectory other than the primary post-critical one and deriving inaccurate velocities from the τ-sum inversion. The sediment–basement boundary is a well-defined break in slope of the energy band at τ, p coordinates of (7.5 s, 210 ms km^{-1}). Data from sonobuoy 354V36 in the τ–p domain (Fig. 7b) display a near-continuous trajectory of quarter-ellipses at τ's between 3.0 and 8.2 s. Another quarter-ellipse of diminished amplitude extends from 9.0 to 10.0 s, and at $p = 140$ ms km^{-1}, or a velocity of 7.1 km s^{-1}, along this energy band we concluded the inversion. Ringing is encountered between τ's of 6.0 and 8.4 s, possibly creating similar problems in the inversion as those previously mentioned. A subtle change in slope of the τ–p trajectory at coordinates of (7.6 s, 210 ms km^{-1}) marks the sediment–oceanic basement interface. The τ-sum inversion solutions for sonobuoys 350V36 and 354V36 are depicted in Figs 6(c) and 7(c), respectively. In both cases it proved impossible to choose a proper τ–p trajectory for the upper ~ 1.5 s of the sediment column from the abundant energy in this region of the τ–p maps. A jump in velocity at ~ 8.1 s two-way travel time associated with the 'red' reflector (Fig. 11) is conspicuous in the two solutions. The red to blue interval has a near-constant velocity of between 4.0 and 4.5 km s^{-1} in both profiles; better resolution is impeded by the ringing factor. A slightly less pronounced velocity discontinuity exists at the interface between sediment and oceanic basement. For sonobuoy 350V36 this transition occurs at 8.9 s two-way travel time; for sonobuoy 354V36, at ~ 8.5 s. The sonic velocity at the top of oceanic basement is 4.8 km s^{-1} in both cases. The solution for sonobuoy 350V36 indicates a rather uniform velocity gradient in oceanic basement extending to ~ 10.0 s two-way travel time ($v = 6.3$ km s^{-1}) where the inversion was concluded. Oceanic basement shows a somewhat different velocity structure from sonobuoy experiment 354V36. Between ~ 8.5 and ~ 9.1 s two-way travel time velocity is a near-constant 4.8 km s^{-1}, and between ~ 9.1 and ~ 9.3 s velocity increases markedly to 6.0 km s^{-1}. Beneath this discontinuity is a less pronounced velocity gradient extending to a velocity of 7.1 km s^{-1} at approximately 10.1 s.

Sonobuoy experiment 359V36 was performed along seismic dip line 86V (Fig. 10), which strikes obliquely to magnetic anomalies identified to the east. The age of the crust is imprecise because it lies within the Jurassic Magnetic Quiet Zone. The SB359V36 data in τ–p space (Fig. 8b) display a continuous band of post-critical reflection energy in intercept times between 2.0 and 8.3 s. We terminated the inversion at $p = 155$ ms km^{-1}, corresponding to a velocity of 6.4 km s^{-1}. Ringing is severe between τ's of 6.2 and 7.7 s, and therefore velocities in the deeper sediments may be subject to error. The sediment–basement

boundary is quite subtle, and occurs at τ–p coordinates of (7.7 s, 180 ms km^{-1}). Fig. 8(c) displays the τ-sum inversion solution for sonobuoy 359V36. The velocity increases more or less gradually to 7.9 s two-way travel time, at which point it increases markedly to a value between 4.0 and 4.1 km s^{-1}. This is the top of the 'red' reflector of Fig. 11, and in this instance the interval between the 'red' and 'blue' reflectors is rather thin. At 8.2 s oceanic basement appears as a dramatic increase in velocity to 5.6 km s^{-1}. From here velocity increases at a lesser rate to the termination of the inversion at 8.7 s two-way travel time.

The final sonobuoy data set analysed by the τ–p method is 380V36. The experiment was performed along multichannel seismic dip line 90V (Fig. 10) at an acute angle to magnetic anomalies M22 and M23 which it traversed. The trajectory of post-critical arrivals is well-defined in the τ–p domain (Fig. 9b) between τ's of 2.0 and 9.0 s. Using assumptions previously described, we terminated the inversion when mantle velocities were attained (p = 125 ms km^{-1}). The deep sediment velocity structure is again uncertain due to ringing between 6.5 and 8.0 s intercept times. A break in slope of the τ–p trajectory at τ = 7.8 s, p = 205 ms km^{-1}, marks the sediment–oceanic basement boundary. The inversion solution for the 380V36 data appears in Fig. 9(c). The uppermost second of sediment did not provide a clear τ–p trajectory. A slight increase in velocity at 8.0 s two-way travel time may be correlated with the 'red' reflector, although a value of 3.5 km s^{-1} is significantly lower than the norm for the top of this interval. At 8.2 s the top of oceanic basement is encountered as a sudden increase in velocity to 4.9 km s^{-1}. Several 'layers' may be present within oceanic basement, but the velocity gradient is generally constant to the point of termination of the inversion at 9.9 s where a velocity of 8.0 km s^{-1} was obtained.

Summarizing the results of the τ–p analyses of the five sonobuoys, the existence of the high-velocity red to blue interval (Fig. 10) immediately overlying oceanic basement is confirmed in at least three of the cases (350V36, 354V36, 359V36) and possibly a fourth (380V36). The layer appears to be of constant velocity at each location. The top of oceanic basement is quite variable in velocity, and the velocity structure of the igneous crust is heterogeneous. In some cases possible layers within the igneous crust are observed; in others a uniform velocity gradient exists. Results from sonobuoy data regarding fine velocity structure within oceanic basement must be sceptically viewed, however, because of the lack of resolution and doubt in discriminating pre- and post-critical energy. In the discussion section we will address the discrepancies between results from the various techniques employed in analysing the sonobuoy data.

Discussion

THE SEDIMENTS

The derivation of velocity–depth functions from interval velocities obtained by the sonobuoy method has been a common exercise over the past decade (Houtz 1974, 1977, 1980a b, 1981; Mountain 1981). One common application of these functions is to convert seismic time sections into depth sections. The values we obtained, v_0 = 1.577 and k = 1.655 km s^{-2} for the Western Somali Basin, and v_0 = 1.637 and k = 1.208 for the Comoros Basin, fall roughly in the middle of values published from a fairly wide distribution of margins and adjacent basins. Examination of the distribution of sonobuoy data included in our study (Fig. 4) demonstrates that the division of the data set into two – the Somali and the Comoros basins – essentially constitutes a partition into a conjugate margin pair according to the tectonic model of Rabinowitz *et al.* (1983). And, despite our inability to confirm or deny the presence of a high-velocity sediment layer in the Comoros Basin from the extant

data, the values for the two basins are not significantly different according to the criteria that Houtz (1981) used to compare velocity functions from conjugate margins. This conclusion is not surprising considering the small size of the basins and the similarity of geological source terrane for the East African and Madagascan margins.

The most interesting feature in the velocity structure of the sedimentary column is the high-velocity layer directly overlying acoustic basement. As previously noted, the mean velocity of the deep sediment layer, as determined by the T^2/X^2 and conventional slope-intercept techniques and confirmed in selected cases by ray tracing, is $4.58 \pm 0.29\,\mathrm{km\,s^{-1}}$. Velocities for the layer were also independently computed for five sonobuoy experiments via the τ–p method, and results from the various techniques do not coincide exactly. SB325V36 did not provide an interval velocity via the T^2/X^2 or slope-intercept methods anywhere near $4.6\,\mathrm{km\,s^{-1}}$ (a velocity of $3.28\,\mathrm{km\,s^{-1}}$ was calculated by the T^2/X^2 technique for the red to blue interval), yet the τ-sum inversion shows a layer characterized by a velocity between 4.0 and $4.3\,\mathrm{km\,s^{-1}}$ immediately above acoustic basement. The τ–p solutions for SB350V36 and SB354V36 yield velocities between 4.0 and $4.5\,\mathrm{km\,s^{-1}}$ for the layer; a velocity of $4.68\,\mathrm{km\,s^{-1}}$ was calculated via the slope-intercept method for SB350V36, and we obtained an interval velocity of $4.06\,\mathrm{km\,s^{-1}}$ by the T^2/X^2 technique from the SB354V36 data. The 'red' reflector yields a slope-intercept refraction velocity of $4.44\,\mathrm{km\,s^{-1}}$ for SB359V36, and the velocity calculated by the τ–p method is between 4.0 and $4.1\,\mathrm{km\,s^{-1}}$. The most conspicuous discrepancy among the various methods occurs in the solutions for SB380V36. The τ–p inversion failed to produce a velocity for the deep layer approaching its value elsewhere: $3.5\,\mathrm{km\,s^{-1}}$ was calculated. T^2/X^2 analysis of the experimental data yielded an interval velocity of $4.51\,\mathrm{km\,s^{-1}}$. T^2/X^2, conventional slope-intercept, and slant-stacked τ–p techniques should produce identical velocity structures for horizontal, laterally homogeneous sediment layers. The discrepancies we observe are probably related to dip, velocity gradients, and/or lateral anisotropy of the sediments. In the absence of reversed profiles and sampling data, such effects are difficult to quantify.

The results from the sonobuoy data analysed by all three methods thus generally confirm the existence of the deep, high-velocity sediment layer. In addition, the τ–p solutions show that velocity is constant through the layer at a given site. Sonobuoy experiments SB350V36, SB354V36 and SB359V36 are relatively consistent among the various techniques. In the other two examples, one technique failed to discern the layer while another succeeded. This highlights the need for a single technique employing pre-critical, critical and post-critical energy in the analysis of seismic data.

Other workers (e.g. Houtz 1974, 1980a, 1981; Mountain 1981) have observed similar deep, high-velocity layers, especially on the passive continental margins bordering the Atlantic Ocean. Possible explanations for these significant velocity jumps in the sedimentary column involve abrupt lithology transitions and/or erosional unconformities which allow lithified, high-velocity sedimentary rocks (which upon removal of overburden tend not to rebound to their velocity at time of deposition) to be in contact with sediments of much lower velocities. Offshore drilling has not yet penetrated the 'red' reflector (Fig. 11) which we identify as the top of the high-velocity layer, and thus we cannot absolutely identify the cause of the observed velocity discontinuity. The velocity of $4.58\,\mathrm{km\,s^{-1}}$ is not in itself diagnostic of any particular lithology. Keen & Cordsen (1981) for example, report velocities in that range for sandstone, shale, dolomite and salt on the Nova Scotian margin at depths of burial similar to those encountered for the layer on the East African margin. We have, however, tentatively identified the layer as the offshore equivalent of a massive Jurassic limestone encountered by drilling onshore in both East Africa and Madagascar (Coffin & Rabinowitz 1982, 1983).

THE IGNEOUS CRUST

Recent reviews of the structure of oceanic basement (Spudich & Orcutt 1980; Fox & Stroup 1981) have emphasized the heterogeneous nature of the igneous crust. These heterogeneities in velocity structure and crustal thickness exist on the scale of several hundreds to thousands of metres both horizontally and vertically, and their resolution is limited by the seismic wavelength ~0.1–2.0 km for our experiments in igneous oceanic crust. Besides the previously mentioned problems and ambiguities inherent to the sonobuoy seismic experiment, ignorance concerning the tectonic origin and evolution of oceanic crust has made it difficult to differentiate between those variations in crustal velocity structure and thickness resulting from syn- and post-accretion tectonic processes. Because our seismic experiments were conducted prior to the firm establishment of a tectonic framework for the Western Somali Basin, they are essentially randomly orientated with respect to any structural fabric resulting from tectonic processes in the basin. Thus the results must be viewed cautiously when attempting to draw any conclusions other than first-order. Nevertheless given the controversy arising from the seismic experiments of Francis *et al.* (1966) regarding the crustal nature of the Western Somali Basin, our results definitely resolve any ambiguities and confirm the oceanic nature of the crust between Madagascar and East Africa.

Although new experimental techniques and methods of data analysis (Spudich & Orcutt 1980; Fox & Stroup 1981) point towards the existence of velocity gradients as opposed to distinct isotropic layers in oceanic basement, the resolution of a seismic experiment is ultimately limited by seismic wavelength, i.e. crustal parameters such as thickness and velocity gradient or discontinuity are defined relative to a wavelength (0.1–2.0 km) over which crustal properties are averaged. Regardless of the analytical method, it is always assumed that the Earth is isotropic vertically for some interval, and is laterally homogeneous. Furthermore, seismic data are invariably noisy due to both experimental problems and crustal heterogeneities, and there is no unique velocity model for a given set of observational seismic data. Due to the nature and quality of our data, we analysed the experiments by traditional T^2/X^2 and slope-intercept methods, occasionally checking the solutions by ray tracing, with the above considerations in mind, and used τ–p transformation and inversion techniques on five of the sonobuoy data sets to evaluate our results. We shall now compare and contrast distinct velocity discontinuity and velocity gradient solutions for oceanic basement obtained through various analytical methods from the same data sets; generally the solutions correlate quite well.

The T^2/X^2 and slope-intercept solution for SB325 (Table 1) describes fairly well a three-layer igneous crust. Layers 2B (5.3 km s^{-1}), 2C (6.1 km s^{-1}), 3 (7.0 km s^{-1}), and mantle (7.7 km s^{-1}) are apparent, the velocities lying within one standard deviation of the mean values listed in Table 3. The total thickness of igneous oceanic crust, commencing at a depth of 8.3 km, is 1.5 s or 4.9 km. The crust–mantle interface lies at a depth of 13.2 km. The τ-sum inversion solution (Fig. 5c) shows the sediment–basement interface appearing at 8.2 km depth, and the velocity for the top of basement is 5.0 km s^{-1}. The inversion was terminated, due to difficulty in distinguishing post-critical from pre-critical arrivals, at 10.4 km depth where a velocity of 6.0 km s^{-1} is encountered. The average velocity gradient for the upper part of the igneous crust is ~0.4 s^{-1}. Comparing the two velocity–depth solutions for SB325V36, we find close agreement on both depth to basement and velocity of the upper igneous crust.

Sonobuoy experiments 350V36 and 354V36, flanking DSDP Site 241 (Figs 4 and 10) and separated by ~55 km, provided solutions not wholly consistent with either layer solutions or gradient models. The conventional slope-intercept solution for SB350V36

Table 3. Summary of velocity analyses.

Layer	V, km/s	N	σ	H, * km; ‡ s	N	σ
High velocity sediment	4.58	47	0.29	-	-	-
Top of acoustic basement	5.40	48	0.37	-	-	-
2	5.83	27	0.27	2.73*	27	0.84
2B	5.42	18	0.19	1.22‡	18	0.39
2C	6.23	18	0.22	1.54*	18	0.47
3	7.03	19	0.25	2.62‡	16	0.71
2 + 3	-	-	-	5.22† 1.62‡	16 16	0.64 0.22
Mantle	7.85	19	0.32	-	-	-

V = velocity.
H = layer thickness in kilometres or seconds of two-way travel time.
N = number of observations.
σ = standard deviation.

provides a velocity in the vicinity of layer 2B (5.4 km s^{-1}), one between 2B and 2C (5.9 km s^{-1}), another lying between 2C and 3 (6.6 km s^{-1}), and a low mantle velocity (7.5 km s^{-1}). Conventional slope-intercept analysis of the data from SB354V36 resulted in a similarly ambiguous velocity–depth profile: a low velocity (4.9 km s^{-1}) was determined for the uppermost part of igneous crust, velocities between 2B and 2C (5.7 km s^{-1}) and 2C and 3 (6.5 km s^{-1}) were obtained, a velocity compatible with layer 3 (7.2 km s^{-1}) was derived, and mantle appears as a 7.8 km s^{-1} layer. For SB350V36, acoustic basement began at 8.8 km and crustal velocities persisted 5.4 km (1.8 s) to 14.2 km depth, the crust–mantle interface. The corresponding values for SB354V36 are 7.7, 5.2 (1.6 s), and 12.9 km. The τ-sum inversion solutions for SB350V36 and SB354V36 give similar depths to and velocities for the top of acoustic basement, 8.5 km and 4.8 km s^{-1}, respectively. Both inversions were terminated before mantle was encountered, SB350V36 at 12.1 km (6.3 km s^{-1}), and SB354V36 at 12.2 km (7.1 km s^{-1}). Velocity gradients derived from the two buoys do not coincide as well; SB350V36 (Fig. 6c) shows a uniform gradient of ~0.4 s^{-1}, while the velocity profile for SB354V36 (Fig. 7c) displays two gradients — ~1.4 s^{-1} between 8.5 and 9.3 km, and ~0.4 s^{-1} between 9.3 and 12.2 km. The various velocity–depth solutions for these two buoys underline the variability inherent in the analysis of seismic data. The slope-intercept and τ-sum inversion solutions for SB350V36 indicate acoustic basement occurring at similar depths, 8.8 and 8.5 km, respectively, but the velocity for the top of the igneous crust is markedly different, 5.4 versus 4.8 km s^{-1}. On multichannel seismic reflection profile 84V (Fig. 10) these velocities appear to correlate with the top of acoustic basement. On the basis of the solutions derived for nearby SB354V36, the choice of the 4.8 km s^{-1} velocity would be favoured. However, the mean velocity for the top of acoustic basement is 5.4 km s^{-1}. Hence ambiguity persists for the true basement velocity in the SB350V36 data. The τ-sum inversion for the buoy was terminated at 12.1 km where the velocity was 6.3 km s^{-1}. At a similar depth the layer solution shows a somewhat similar velocity of 6.6 km s^{-1}. The layer and τ-sum inversion solutions for SB354V36 indicate similar velocities for the top of acoustic basement, 4.9 and 4.8 km s^{-1}, respectively, but differing velocity profiles in the sediment column result in a significant discrepancy in total depth to basement, 7.7 versus

8.5 km. On comparison with other seismic solutions from the region, the latter τ-sum inversion value is preferable. At the depth of termination, 12.2 km, of the τ-sum inversion, the velocity obtained was 7.1 km s^{-1}. At a comparable depth the conventional slope-intercept analysis yields a velocity of 7.2 km s^{-1}.

Velocity profiles for SB359V36 produced by the two analytical methods (Table 1, Fig. 8c) are in close agreement. Conventional slope-intercept analysis yields four layers correlative with 2B (5.3 km s^{-1}), 2C (6.4 km s^{-1}), 3 (7.0 km s^{-1}) and mantle (7.6 km s^{-1}). Integrated igneous crustal thickness is 5.2 km (1.6 s), its upper surface occurring at 7.9 km and mantle appearing at 13.1 km. The τ-sum inversion solution shows igneous basement commencing at 8.0 km, and the profile is reliable to 9.2 km where a velocity of 6.4 km s^{-1} was reached, identical to the value attained at that depth by the layer solution. The gradient for the upper part of oceanic crust is 0.7 s^{-1}.

Data quality from SB380V36 did not allow construction of a velocity–depth profile for basement via slope-intercept analysis; however, the τ-sum inversion (Fig. 9c) did produce a velocity profile. The top of basement (4.9 km s^{-1}) lies at 7.9 km depth, and oceanic crust extends 4.9 km (1.7 s) to mantle (8.0 km s^{-1}) at a depth of 12.8 km. Two gradients are apparent within the igneous crust, ~0.8 s^{-1} between 7.9 and 9.0 km, and ~0.6 s^{-1} between 9.0 and 12.8 km. The break in gradient occurs at a velocity of 5.9 km s^{-1}.

Overall the velocity solutions we obtained through analysis of the seismic data present a picture of oceanic crust compatible with both layer and gradient models developed from Atlantic and Pacific data (Spudich & Orcutt 1980; Fox & Stroup 1981). Because the crust in the study area is extremely old, between ~165 and ~130 Ma (Rabinowitz *et al.* 1983), low velocities and sharp gradients associated with the top of oceanic basement, i.e. layer 2A, are absent, presumably due to hydrothermal processes and metamorphism resulting in higher velocities for the upper portion of basement. The crustal model which emerges from our data includes layers 2B and 2C, a region of sharper velocity gradients (~0.4 to ~1.4 s^{-1}), as well as layer 3, with gradients of ~0.4 to ~0.6 s^{-1}, and mantle.

Intriguing are the departures from 'normal' oceanic crustal structure discovered through the velocity analyses. Several workers (Stoffa *et al.* 1980; Talwani *et al.* 1982; Mutter 1982; Mutter *et al.* 1984) have noted from both reflection and refraction data that the total thickness of igneous oceanic crust, both old and young, at various locations in the world's oceans, approximates 2.0 s of two-way travel time. As previously mentioned, our study comprising 16 sonobuoy experiments resulted in a value of 1.62 ± 0.22 s (5.22 ± 0.64 km) for the total igneous crustal thickness in the Western Somali Basin. Most models of 'normal' oceanic crustal formation and evolution (summarized by Cann 1981; Fox & Stroup 1981) predict a positive correlation between crustal thickness and age, and one would thus anticipate a thick igneous crustal section for the basin. Spreading rates derived from marine magnetic anomalies are in the low range (half-rates = 1.7–1.8 cm yr^{-1}; Rabinowitz *et al.* 1983), and there is no evidence of fracture zones or other anomalies which could possibly account for a condensed crustal section.

EAST AFRICA SEISMIC TRANSECT

In Fig. 2 we present two transects (in depth) across the East African continental margin (see Fig. 4 for station locations). The upper section is taken from Francis (1964) and Francis *et al.* (1966), and is based on the results of five sonobuoy explosion refraction experiments performed in 1963. The lower section is our revised transect employing all available velocity solutions as well as multichannel seismic reflection data. Incorporated sonobuoy experiments are identified on the top of each transect. The inferred geological column on the left

of the upper figure is based on onshore stratigraphy and was provided by British Petroleum to Francis, and the coloured reflector scheme of the bottom figure is based on both DSDP 241 and onshore stratigraphy as described by Coffin & Rabinowitz (1982, 1983) and summarized in the figure caption. The revised transect (lower figure) shows structures similar to those found on many passive margins around the world. Mantle, layer 3, and layer 2 (Fig. 15) all dip landward and disappear beneath a thick wedge of continental rise sediments.

A significant interpretation of the Francis (1964) and Francis *et al.* (1966) works, cited frequently in Madagascar–Africa reconstruction studies, was that Karroo sediments extended for hundreds of kilometres east from the African mainland on to crust of the Western Somali Basin. The results of this study indicate that the crust seaward of SB365V36 (Figs 2 and 4) is of oceanic nature, created while Madagascar and Africa separated. The end of Karroo deposition may be correlated with the initiation of seafloor spreading between Madagascar and Africa (Coffin & Rabinowtiz 1986a,b), and hence there are probably no Karroo-age sediments extending seaward of SB365V36. The inferred Jurassic and Cretaceous thicknesses of the upper section (Fig. 2) are probably in error; it is probable that the bulk of the sediment column (in excess of 8 km beneath the continental rise) is of those ages.

Conclusions

(1) We have determined two sets of values for the equation, $v = v_0 + Kt$, applicable to the sedimentary columns in the Western Somali Basin ($v_0 = 1.577 \pm 0.280$ km s^{-1}, $K = 1.655$ km s^{-2}) and the Comoros Basin ($v_0 = 1.637 \pm 0.224$ km s^{-1}, $K = 1.208$ km s^{-2}). The values fall in the middle of those reported in the literature from a fairly wide distribution of margins and adjacent basins around the world. The Comoros and Western Somali basin figures are not significantly different, emphasizing the similar palaeoenvironment and provenance of the sediments throughout much of the basins' histories. Applying the values to digitized seismic reflection data we have compiled total sediment thickness and depth to basement maps which document sediments in excess of 8 and 5 km on the conjugate East African and Madagascan margins, respectively, and highlight tectonic anomalies in the region. These maps are described in full detail elsewhere (Coffin & Rabinowitz 1986a).

(2) A deep, high-velocity (4.58 ± 0.29 km s^{-1}) isotropic layer defined by 47 sonobuoy experiments overlies acoustic basement along the East African continental margin. Such velocity discontinuities and high-velocity sediment layers have been observed on other passive margins, and our acoustic stratigraphic studies (Coffin & Rabinowitz 1986a) indicate that the top of the reflection sequence correlative with the isotropic layer is not an erosional unconformity. We interpret the layer to be a distinct lithological unit infilling basement troughs which is the offshore equivalent of a massive Jurassic limestone sequence observed on land seismic sections and sampled by drilling.

(3) The crust of the Western Somali Basin and its sub-basin, the Comoros Basin, is decidedly oceanic in character, resolving controversies of the past. The top of igneous crust displays a mean velocity of 5.40 ± 0.37 km s^{-1} from 48 sonobuoy experiments ($N = 48$), and seismic layer 2A is not present. Both the high velocity for the uppermost portion of oceanic crust and the corresponding absence of layer 2A are cosmopolitan characteristics of old, in this case ~165–~130 Ma, oceanic crust. Seismic layers 2B, 2C, 3 and mantle are present with mean velocities of 5.42 ± 0.19 ($N = 18$), 6.23 ± 0.22 ($N = 18$), 7.03 ± 0.25 ($N = 19$), and 7.85 ± 0.32 ($N = 19$) km s^{-1}, respectively. It was not possible to resolve layers 3A and 3B through any of the analytical methods. The determined velocities, with the exception of the mantle, fall in the high end of the range of values reported in global summaries (e.g. Fox & Stroup 1981), which is expected given the age of the crust, τ–p analysis of the sonobuoy

data reveal a steeper velocity gradient (~ 0.4 to ~ 1.4 s^{-1}) in layer 2 than in layer 3 (~ 0.4 to ~ 0.6 s^{-1}). Similar gradients have been reported on the basis of limited results from relatively young crust in the Pacific Ocean (Spudich & Orcutt 1980). Mantle velocities are generally slightly lower than those reported by Fox & Stroup, which were generally derived from data acquired and analysed by techniques similar to those used in this study. We speculate that the differences in the velocities of mantle and layer 3 narrow in very old oceanic crust (and may be related to high-velocity basal crustal layers). More research on the crust–mantle boundary is clearly needed to test the ubiquity of this observation and concept.

(4) The thicknesses of layers 2 and 3 are 2.73 ± 0.84, and 2.62 ± 0.71 km, respectively, again within the range of Fox & Stroup's (1981) world-wide figures. In terms of two-way travel time, the total thickness of igneous oceanic crust is 1.62 ± 0.22 s, approximately 20 per cent thinner than values remarked upon elsewhere (see text for references). This result is significant for two primary reasons: (a) the data set, consisting of 16 sonobuoy experiments all displaying strong mantle headwaves, constitutes a large number of determinations of integrated oceanic crustal thickness from a limited geographical area, and (b) the experiments were performed on the oldest identified oceanic crust in the Indian Ocean, and among the oldest world-wide. The value of 1.62 ± 0.22 s establishes a baseline for further analyses. including the modelling of oceanic crustal formation and evolution in nascent ocean basins.

(5) A revised depth section across the East African margin shows typical rifted passive margin structure, including oceanic basement and mantle dipping landward, and a thick wedge of sediments beneath the continental rise. Karroo sediments in all likelihood do not extend offshore East Africa into the Western Somali Basin, refuting a piece of evidence that has been vital to many reconstruction efforts fitting Madagascar in Gondwanaland in palaeo-positions other than adjacent to Somalia, Kenya and Tanzania.

Acknowledgments

We thank the officers, crew, and scientists on the R/V *Vema* for their support and cooperation in gathering the data. John Mutter provided advice on τ–p analysis, Emilio Vera on ray-tracing, Joyce Alsop on seismic data processing, and Tim Francis supplied a copy of his PhD thesis. Greg Mountain and Peter Naumoff were invaluable in helping to digitize and process the seismic records used in sediment and crustal thickness maps. We are grateful to John Mutter, James Cochran, Dennis Hayes, James Hays and two anonymous reviewers for critically reading the manuscript. Ana Maria Alvarez, Carl Brenner, Milly Giarratano and Mary Ann Stage ably provided technical services. This work was supported by NSF OCE 79-19389. Lamont–Doherty contribution No. 3977.

References

Bunce, E. T. & Molnar, P., 1977. Seismic reflection profiling and basement topography in the Somali Basin: possible fracture zones between Madagascar and Africa, *J. geophys. Res.*, **82**, 5305–5311.

Cann, J. R., 1981. Basalts from the ocean floor, in *The Sea*, 7, 363–390, ed. Emiliani, C., Wiley, New York.

Coffin, M. & Rabinowitz, P., 1982. A multichannel seismic transect of the Somalian continental margin, in *Proc. Offshore Technol. Conf.*, **2**, 421–430.

Coffin, M. & Rabinowitz, P., 1983. East African continental margin transect, in *Seismic Expression of Structural Styles*, ed. Bally, A. W., *AAPG Studies in Geol.*, **15**, 2.3.3–22–30.

Coffin, M. & Rabinowitz, P., 1986a. Evolution of the conjugate East African–Madagascan margins and the Western Somali Basin, in preparation.

Coffin, M. & Rabinowitz, P., 1986b. The fit of Madagascar in Gondwanaland, in preparation.

Diebold, J. B., 1980. The travel time equation, tau-*p* mapping and inversion of common midpoint seismic data with applications to the geology of the Venezuela Basin, *PhD thesis,* Columbia University.

Diebold, J. B. & Stoffa, P. L., 1981. The travel-time equation, tau–*p* mapping, and inversion of common midpoint data. *Geophysics,* **46,** 238–254.

Diebold, J., Stoffa, P., Buhl, P. & Truchan, M., 1981. Venezuela Basin crustal structure, *J. geophys. Res.,* **86,** 7901–7923.

Emerick, C. M. & Duncan, R. A., 1982. Age progressive volcanism in the Comores Archipelago, western Indian Ocean and implications for Somali plate tectonics, *Earth planet. Sci. Lett.,* **60,** 415–428.

Ewing, J., 1963. Elementary theory of seismic refraction and reflection measurements, in *The Sea,* **3,** 3–19, ed. Hill, M. N., Wiley, New York.

Fox, P. J. & Stroup, J. B., 1981. The plutonic foundation of the oceanic crust, in *The Sea,* 7, 119–218, ed. Emiliani, C., Wiley, New York.

Francis, T. J. G., 1964. Seismic observations at sea with long range recording buoys, *PhD thesis,* University of Cambridge.

Francis, T. J. G., Davies, D. & Hill, M. N., 1966. Crustal structure between Kenya and the Seychelles, *Phil. Trans. R. Soc. A,* **259,** 240–261.

Houtz, R., 1974. Preliminary study of global sediment sound velocities from sonobuoy data, in *Physics of Sound in Marine Sediments,* pp. 519–535, ed. Hampton, L., Plenum Press, New York.

Houtz, R. E., 1977. Sound–velocity characteristics of sediment from the eastern South American margin, *Bull. geol. Soc. Am.,* **88,** 720–722.

Houtz, R., 1980a. Comparison of velocity–depth characteristics in western North Atlantic and Norwegian Sea Sediments, *J. acoust. Soc. Am.,* **68,** 1409–1919.

Houtz, R. E., 1980b. Results and methods used to determine the acoustic properties of the Southeast Asian margins, in *Bottom-Interacting Ocean Acoustics,* pp. 99–109, eds Kuperman, W. A. & Jensen, F. B., Plenum Press, New York.

Houtz, R., 1981. Comparison of sediment sound–velocity functions from conjugate margins. *Bull. geol. Soc. Am.,* **92,** 262–267.

Keen, C. E. & Cordsen, A., 1981. Crustal structure, seismic statigraphy, and rift processes of the continental margin off eastern Canada: ocean bottom seismic refraction results off Nova Scotia, *Can. J. Earth Sci.,* **18,** 1523–1538.

Kent, D. V. & Gradstein, F. M., 1985. A cretaceous and jurassic geochronology, *Bull. geol. Soc. Am.,* **96,** 1419–1427.

Le Pichon, X., Ewing, J. & Houtz, R., 1968. Deep-sea sediment velocity determination made while reflection profiling, *J. geophys. Res.,* **73,** 2597–2614.

Lort, J., Limond, W., Segoufin, J., Patriat, P., Delteil, J. & Damotte, B., 1979. New seismic data in the Mozambique Channel, *Mar. geophys. Res.,* **4,** 71–89.

Matthews, D. J., 1939. *Tables of the Velocity of Sound in Pure Water and Sea Water for Use in Echo Sounding and Sound Ranging,* Admiralty Office, London.

Mountain, G. S., 1981. Stratigraphy of the Western North Atlantic based on the study of reflection profiles and DSDP results, *PhD thesis,* Columbia University in the City of New York.

Mutter, J. C., 1982. Rifting of the Norwegian margin and young ocean basin accretion dynamics in the Norwegian–Greenland Sea, *PhD thesis,* Columbia University.

Mutter, J. C., Talwani, M. & Stoffa, P., 1984. Evidence for a thick oceanic crust adjacent to the Norwegian margin, *J. geophys. Res.,* **84,** 483–502.

Rabinowitz, P. D., Coffin, M. & Falvey, D., 1983. The Separation of Madagascar and Africa, *Science,* **220,** 67–69.

Simpson, Schlich *et al.* 1974. *Initial Reports of the Deep Sea Drilling Project,* **25,** U.S. Government Printing Office, Washington DC.

Spudich, D. & Orcutt, J., 1980. A new look at the seismic velocity structure of the oceanic crust, *Rev. Geophys. Space Phys.,* **18,** 627–645.

Stoffa, P. L., Buhl, P., Diebold, J. B. & Wenzel, F., 1981. Direct mapping of seismic data to the domain of intercept time and ray parameter. A plane wave decomposition, *Geophysics,* **46,** 255–267.

Stoffa, P. L., Buhl, P., Herron, T. J., Kan, T. K. & Ludwig, W. J., 1980. Mantle reflections beneath the crustal zone of the East Pacific Rise from multi-channel seismic data, *Mar. Geol.,* **35,** 83–97.

Talwani, M., Stoffa, P., Buhl, P., Windisch, C. & Diebold, J. B., 1982. Seismic multichannel towed arrays in the exploration of the oceanic crust, *Tectonophys.,* **81,** 273–300.